Characterizing methane emission hotspots from thawing permafrost

Clayton Drew Elder[1], David Ray Thompson[1], Andrew K Thorpe[1], Hrishikesh Arvind Chandanpurkar[2], Philip J. Hanke[3], Nicholas Hasson[3], Stephanie R. James[4], Burke J Minsley[5], Neal Pastick[6], David Olefedt[7], Katey Walter Anthony[3], and Charles E. Miller[8]

[1]Jet Propulsion Laboratory, California Institute of Technology
[2]NASA Jet Propulsion Laboratory
[3]University of Alaska Fairbanks
[4]U.S. Geological Survey
[5]United States Geological Survey
[6]KBR, Inc
[7]University of Alberta
[8]Jet Propulsion Laboratory

November 22, 2022

Abstract

Methane (CH_4) emissions from climate-sensitive ecosystems within the northern permafrost region represent a large but highly uncertain source, with current estimates spanning a factor of seven (11 – 75 Tg CH_4 yr^{-1}). Accelerating permafrost thaw threatens significant increases in pan-Arctic CH_4 emissions, amplifying the permafrost carbon feedback. We used airborne imaging spectroscopy with meter-scale spatial resolution and broad coverage to identify a previously undiscovered CH_4 hotspot adjacent to an intensively studied thermokarst lake in interior Alaska. Hotspot emissions were confined to $< 1\%$ of the 10 ha study area. Ground-based chamber measurements confirmed average daily fluxes of 1,170 mg CH_4 m^{-2} d^{-1}, with extreme daily maxima up to 24,200 mg CH_4 m^{-2} d^{-1}. Ground-based geophysics measurements revealed thawed permafrost at and directly beneath the CH_4 hotspot, extending to a depth of ˜15 m, indicating that the intense CH_4 emissions likely originated from recently thawed permafrost. Emissions from the hotspot accounted for ˜40% of total diffusive CH_4 emissions from the entire study area. Combining these results with hotspot statistics from our 70,000 km^2 airborne survey across Alaska and northwestern Canada, we estimate that terrestrial thermokarst hotspots currently emit 1.1 (0.1 – 5.2) Tg CH_4 yr^{-1}, or roughly 4% of the annual pan-Arctic wetland budget from just 0.01% of the northern permafrost land area. Our results suggest that significant proportions of pan-Arctic CH_4 emissions originate from disproportionately small areas of previously undetermined thermokarst emissions hotspots, and that pan-Arctic CH_4 emissions may increase non-linearly as thermokarst processes increase under a warming climate.

Characterizing methane emission hotspots from thawing permafrost

Authors:

Clayton D. Elder[1], David R. Thompson[1], Andrew K. Thorpe[1], Hrishikesh Chandanpurkar[1], Philip J. Hanke[2], Nicholas Hasson[2], Stephanie R. James[3], Burke Minsley[3], Neal J. Pastick[4], David Olefedt[5], Katey M. Walter Anthony[2], Charles E. Miller[1]

Correspondence to:

C. D. Elder, clayton.d.elder@jpl.nasa.gov

Affiliations:

[1]Jet Propulsion Laboratory, California Institute of Technology, Pasadena, CA, USA, [2]Water and Environmental Research Center, University of Alaska, Fairbanks, AK, USA, [3]Geology, Geophysics, and Geochemistry Science Center, U.S. Geological Survey, Denver, CO, USA, [4]KBR, Contractor to the U.S. Geological Survey, Earth Resources Observation and Science Center, Sioux Falls, SD, USA, [5]Department of Renewable Resources, University of Alberta, Edmonton, AB, CAN

Key points:

- Repeat airborne spectral imaging geolocated a thermokarst CH_4 hotspot with ground-validated emissions >10 g CH_4 m^{-2} d^{-1}.
- Hotspot CH_4 emissions arose from <1% of our 10 ha thermokarst lake study area but comprised ~40% of the total diffusive emissions.
- Ground-based and airborne observations suggest thermokarst hotspots emit roughly 1.1 Tg CH_4 yr^{-1} or 4% of pan-Arctic wetland CH_4 emissions.

Abstract

Methane (CH_4) emissions from climate-sensitive ecosystems within the northern permafrost region represent a large but highly uncertain source, with current estimates spanning a factor of seven (11 – 75 Tg CH_4 yr^{-1}). Accelerating permafrost thaw threatens significant increases in pan-Arctic CH_4 emissions, amplifying the permafrost carbon feedback. We used airborne imaging spectroscopy with meter-scale spatial resolution and broad coverage to identify a previously undiscovered CH_4 hotspot adjacent to an intensively studied thermokarst lake in interior Alaska. Hotspot emissions were confined to < 1% of the 10 ha study area. Ground-based chamber measurements confirmed average daily fluxes of 1,170 mg CH_4 m^{-2} d^{-1}, with extreme daily maxima up to 24,200 mg CH_4 m^{-2} d^{-1}. Ground-based geophysics measurements revealed thawed permafrost at and directly beneath the CH_4 hotspot, extending to a depth of ~15 m, indicating that the intense CH_4 emissions likely originated from recently thawed permafrost. Emissions from the hotspot accounted for ~40% of total diffusive CH_4 emissions from the entire study area. Combining these results with hotspot statistics from our 70,000 km^2 airborne survey across Alaska and northwestern Canada, we estimate that terrestrial thermokarst hotspots currently emit 1.1 (0.1 – 5.2) Tg CH_4 yr^{-1}, or roughly 4% of the annual pan-Arctic wetland budget from just 0.01% of the northern permafrost land area. Our results suggest that significant proportions of pan-Arctic CH_4 emissions originate from disproportionately small areas of previously undetermined thermokarst emissions hotspots, and that pan-Arctic CH_4 emissions may increase non-linearly as thermokarst processes increase under a warming climate.

Plain language summary

We conducted high resolution airborne surveys of near-surface CH_4 (powerful greenhouse gas) anomalies in Alaska and northwestern Canada during the summers of 2017-2019 as part of NASA's Arctic Boreal Vulnerability Experiment (ABoVE). These measurements provided fine-scale resolution for the remote detection of CH_4 emission hotspots from natural Arctic environments. Repeated flights over Big Trail Lake near Fairbanks, AK revealed a previously undiscovered CH_4 hotspot at this intensive study site. Ground-based measurements confirmed extremely high surface-to-atmosphere fluxes (> 10 g CH_4 m^{-2} d^{-1}) at this location, on the shore of a permafrost-thaw pond that formed after 1963. Geophysical surveys confirmed the presence of thawed permafrost at the hotspot and in a sub-surface thawed region that extends ~15 m beneath the surface. We hypothesize that the recent permafrost thaw and subsidence (thermokarst) made soils with highly decomposable organic carbon available for microbial metabolism, conversion into CH_4, and enhanced emission to the atmosphere. Extrapolating our observed CH_4 hotspot fluxes and broad-area hotspot distribution statistics with published values for the total area of thermokarst features across the pan-Arctic, we estimate that thermokarst CH_4 hotspots constitute less than 0.01% of the pan-Arctic land area, but contribute 1.1 (range of estimates = 0.1 – 5.2) Tg CH_4 yr^{-1}, or roughly 4% of the annual pan-Arctic wetland emissions. We further hypothesize that Arctic CH_4 emissions may grow significantly in the future with anticipated increases in thermokarst across the permafrost landscape.

Keywords

Arctic, methane, thermokarst, permafrost, hotspots, remote sensing, emissions upscaling

1. Introduction

Pronounced warming of the northern high-latitudes is causing rapid permafrost thawing and subsequent collapse of ground surfaces (thermokarst) (Farquharson et al., 2019; Lewkowicz & Way, 2019), threatening the stability of the 1,300 - 1,600 Pg permafrost carbon (C) reservoir (Schuur et al., 2015). The effect of widespread thermokarst and/or abrupt thaw on pan-Arctic greenhouse gas (GHG) emissions is poorly understood despite its potential impact to global climate. Turetsky et al. (2020) estimate that abrupt permafrost thaw processes may add an additional 40 ± 10% to net C emission or 0.30 W m^{-2} net radiative forcing beyond that expected from gradual deepening of the seasonally thawed active layer through year 2300. Uncertainties in future anthropogenic C emissions, along with uncertainties inherent to modelling heterogeneous Arctic landscapes, result in broad disagreement on both the sign and magnitude of forecasted net C exchange from permafrost regions through the 23rd century (McGuire et al., 2018). This emphasizes the need to improve our observational capabilities of the Arctic C cycle, especially for CH_4 emissions due to their 25-30 greater potency as a greenhouse gas (GHG) compared to carbon dioxide (CO_2) on a 100-yr timescale. This potency means CH_4 emissions from abruptly thawing permafrost may constitute 50% of the total future radiative forcing from permafrost emissions, despite emissions being four times lower than CO_2 (Turetsky et al., 2020). Extreme spatiotemporal variability of CH_4 emissions from heterogenous permafrost environments further compounds the uncertainty related to forecasting the permafrost C feedback in a rapidly warming Arctic. Constraining these uncertainties in current and future thermokarst-related CH_4 emission estimates will require advances in fine-scale, process-oriented modeling of the key regulators of emissions developed in concert with high resolution, broad-area emissions monitoring.

92 Growing evidence links high CH_4 emissions, particularly ebullition, to intense areas of
93 abrupt permafrost thaw and mobilization of highly labile and ancient permafrost organic carbon
94 (Serikova et al., 2019; Walter Anthony et al., 2016). However, the extent and impact of abrupt
95 thaw and/or thermokarst emissions on the pan-Arctic CH_4 budget is unclear. This is especially so
96 since young/contemporary carbon sources dominate whole-lake and diffusive wetland GHG
97 emissions in some high latitude studies (Cooper et al., 2017; Dean et al., 2020; Elder et al., 2018),
98 and some evidence suggests that Arctic CH_4 emissions have likely not increased significantly over
99 the last 40 years (Sweeney et al., 2016). Estimating annual pan-Arctic CH_4 emissions is
100 challenging due to a paucity of in situ observations and detailed geospatial datasets (e.g. wetland
101 type and distribution, thermokarst landforms, soil moisture, etc.) needed to accurately scale
102 emission patterns across heterogeneous permafrost landscapes (Bloom et al., 2017; Morel et al.,
103 2019). A key contributor to this uncertainty is the propensity of large proportions of total emissions
104 to originate from tiny fractions of the landscape, further challenging field research and modelling
105 efforts (Turetsky et al., 2020). As a result, Arctic CH_4 emission estimates span a factor of seven
106 across process-based and inversion models (11 – 75 Tg CH_4 yr^{-1}) and flux upscaling (21-54 Tg
107 CH_4 yr^{-1}) (McGuire et al., 2012; Peltola et al., 2019). Constraining budget estimates and model
108 behavior will require a combination of expanded process-oriented field observations,
109 determination of key spatial metrics, and mechanistic insights derived from complimentary high-
110 resolution remote sensing (Elder, Thompson, et al., 2020).
111 Here we combined metrics from a synoptic-scale airborne CH_4 hotspot survey of Alaska
112 and western Canada (Elder, Thompson, et al., 2020) with new ground-based and airborne remote
113 sensing observations of permafrost structure and extreme CH_4 emissions at a thermokarst lake, 8
114 km north of Fairbanks, AK to estimate CH_4 fluxes attributable to active thermokarst morphology

across the northern permafrost domain. In this work, we utilize an airborne CH_4 hotspot dataset, unprecedented in resolution and coverage, to investigate and estimate the influence of thermokarst on CH_4 hotspot emissions from plot scales to pan-Arctic scales. Where Elder, Thompson, et al. (2020) took a broad-scale statistical approach to investigate emergent hotspot patterns, this study investigates the mechanisms behind hotspot emissions, quantifying hotspot flux rates, apportioning them in the context of our thermokarst lake study environment, and extrapolating to pan-Arctic scales. Our study demonstrates the ability to detect anomalous CH_4 fluxes at high resolution across large spatial domains, which is critical for informing ground-based study and for accurate spatial upscaling. Our findings represent a unique observation-based approach to estimating contemporary pan-Arctic terrestrial thermokarst CH_4 emissions, which are expected to dramatically increase within the next century.

2. Methods

2.1 CH_4 patterns at high spatial resolution across broad scales

NASA's Arctic Boreal Vulnerability Experiment (ABoVE) surveyed over 70,000 km^2 of Alaska and northwestern Canada with the Next Generation Airborne Visible/Infrared Imaging Spectrometer (AVIRIS-NG) during the summers of 2017, 2018, and 2019 (C. E. Miller et al., 2019). AVIRIS-NG was installed on a KingAir B-200 (Dynamic Aviation, tail number N53W) which flew at altitudes from 2 - 6 km above ground level (AGL), providing ground sampling distances (pixel dimensions) of 2 - 6 m.

AVIRIS-NG maps CH_4 hotspots with meter-scale spatial resolution by measuring shortwave infrared (SWIR) CH_4 absorption features present in surface-reflected solar radiation. The remote measurement used a matched filter approach presented in (Thompson, Leifer, et al.,

2015), and deployed in multiple subsequent campaigns (Cusworth et al., 2020; Duren et al., 2019; Elder, Thompson, et al., 2020; Frankenberg et al., 2016; Thorpe et al., 2020). A complete description appears in the Supporting Methods. The remote mapping process produced maps quantifying the CH_4 absorption above background levels in between the sensor and the surface in integrated concentration path-length units, ppm m. Subsequent analyses of these CH_4 enhancement images identified "hotspots," which we operationally defined as clusters of enhanced pixels with a minimum of 2500-3000 ppm m excess CH_4 above background concentrations. This threshold typically represented a minimum signal-to-noise ratio of three to four. In lower altitude ABoVE surveys (< 3 km AGL), AVIRIS-NG was more sensitive to column CH_4 absorption, however scene heterogeneity often inflated spectrometer noise. While AVIRIS-NG can observe CH_4 over open water in sun glint conditions (Thorpe et al., 2013, 2014), flight lines in this study were not planned to optimize glint. Thus, our CH_4 measurements were limited to terrestrial surfaces leading up to the water's edge. Therefore, the hotspots discussed here should be considered terrestrial or littoral.

2.2 Remote detection of hotspots at Big Trail Lake

During the 2018 and 2019 ABoVE airborne campaigns (AAC), AVIRIS-NG targeted Big Trail Lake (BTL) (64.91940°, -147.82222°) and its adjacent thermokarst pond (informally named "Eastside Pond" hereafter). These sites benefited both from ongoing ground validation and CH_4 flux monitoring (Elder, Thompson, et al., 2020), and their location along the flight approach to Fairbanks International Airport, the regional base of operations for AVIRIS-NG. The latter allowed for 17 successful overflights of BTL at multiple survey altitudes and sun angles, enabling repeated hotspot analysis. See Supporting Methods for a description of the CH_4 retrieval process.

2.3 Site description of Big Trail Lake

BTL is an active thermokarst lake recently formed atop degrading ice-rich yedoma soils on public lands in the Goldstream Creek watershed of interior Alaska. Airborne photographic records indicate that BTL formed from a fen wetland sometime between 1949 and 1967 and has since expanded to 4.15 ha (Walter Anthony et al., 2018). Multiple rivulet streams draining surrounding fens, including a remnant flow path of Goldstream Creek, feed the Eastside Pond. In some of the inlet streams, the water flows ephemerally. Water leaves the pond through a 10-m-wide channel feeding into the east side of BTL. A narrow outlet drains BTL's main lake body from the southwest corner. The shallow portions of the main body of BTL support communities of macrophytes including abundant *Potamogeton*. The shorelines of BTL and Eastside Pond have abundant hydrophytic vegetation communities (i.e. genus: *Typha*, *Carex*, *Equisetum*, *Juncus*, etc.), many with aerenchyma that can serve as a conduit for CH_4 to escape to the atmosphere (Ström et al., 2003).

A persistent remotely sensed CH_4 hotspot was detected along the eastern shoreline of the Eastside Pond (Figure 1). This shoreline is characterized by a rapid transition from non-emergent and emergent littoral vegetation to upland vegetation species along steep erosional banks (Figure S1). Two to three rivulet streams, which drain the small fen ~70 m to the east, converge at the location of the CH_4 hotspot along the eastern margin of the Eastside Pond and likely contribute to enhanced thermokarst at the site. The Eastside Pond initially formed sometime between 1967 and 1985 (Walter Anthony et al., 2018). We estimate from aerial photography in Walter Anthony et al. (2018) that the Eastside Pond has expanded by 0.5 – 1 m yr^{-1} since formation. Its formation was likely influenced to some extent by the development of an unpaved, single-lane access road which was built in the mid 20th century. Despite the road being un-maintained and impassable for many years due to flowing water and seasonal flooding, it still serves as a recreational path to cross

183 country skiers and mushers when the Eastside Pond freezes in winter. Multiple other thermokarst
184 ponds occur along the old ~1 km road, however it is unknown to what extent the road's presence
185 affects contemporary thermokarst or CH_4 emissions in the thermokarst-rich Goldstream Valley.

186 **2.4 Ground-based enhancement and flux surveys**

187 We monitored CH_4 fluxes at BTL via repeat chamber-flux measurements along five shore-
188 to-forest transects since summer 2018 (Elder, Hanke, et al., 2020). We added hotspot monitoring
189 measurements near the Eastside Pond in July 2019. These measurements validated the persistent
190 hotspot detected near the Eastside Pond in AVIRIS-NG overflights since July 2019. Additionally,
191 we performed a ground-based CH_4 enhancement survey on July 6th, 2019 between 13:25 – 17:15
192 Alaska Daylight Time (AKDT), approximately 2 hours following an AVIRIS-NG overflight and
193 hotspot detection at the Eastside Pond (Figure 1). During the ground-based enhancement survey,
194 atmospheric CH_4 concentrations were measured at 1 Hz with a Los Gatos Ultra-Portable
195 Greenhouse Gas Analyzer (UGGA) (ABB INC., 85 Quebec City, CA) in the free air at
196 approximately 0.5 m AGL and on a ~10 cm s^{-1} snaking transect starting in the southwest and
197 working northeast of the hotspot region (Figure 2). Wooden planks were used as footpaths in
198 sensitive environments to minimize disturbance. The geolocation accuracy of mapped CH_4
199 concentrations is estimated to be ± 5 m, with uncertainties dominated by lags in GPS updates
200 during the walking survey.

201 The hotspot fluxes reported here were measured on 5 days in between 7/7/19 and 9/17/19,
202 and on 12/14/19, resulting in 74 total observations from the Eastside Pond hotspot region.
203 Diffusive fluxes were measured as in Elder, Thompson, et al. (2020), except that permanent
204 aluminum chamber-collars were installed to 3-5 cm depth at long-term flux monitoring locations
205 near the hotspot and other locations of BTL. Additionally, more-mobile chambers, constructed

206 from plastic five-gallon buckets with bottoms removed, and resealable air-tight lids (Gamma Seal
207 Lid, Encore Plastics, Sandusky, OH, USA) (Figure S2) were installed at hotspot flux monitoring
208 locations (Figure 2). Buckets were installed such that 2-5 cm of the open bottom was submerged
209 in saturated sediments to create a hermetic seal with the surface. These hotspot monitoring
210 positions (n = 12) were equally spaced 3-4 m apart on sparsely-vegetated or bare, saturated
211 surfaces along the southeastern shoreline of the Eastside Pond where the water table was nearest
212 to the surface, or where we expected the highest diffusive fluxes. Buckets were left in place, sans
213 lid, for at least 24 hours before fluxes were measured and remained in place until removal just
214 before seasonal freeze up. As singular bucket was placed on the snow surface at the hotspot
215 location to observe fluxes on 12/14/19. The chamber volume was corrected for snow density inside
216 the chamber for this measurement. During all flux measurements, lids fitted with ¼" PVC valves
217 were carefully screwed into the top of each bucket, creating an air-tight closed chamber to
218 recirculate air through the UGGA. Lids were removed after each measurement. Diffusive fluxes
219 were calculated from the ideal gas law using chamber volume, temperature, atmospheric pressure
220 measured via a LI-COR LI7700 (LI-COR Inc., Lincoln, Nebraska, USA) operating mid-BTL, and
221 linear CH_4 concentration change ($R^2 > 0.985$ correlation to linear least squares fit) for a minimum
222 of 45 seconds (45 observations) within the chamber. Observations with non-linear concentration
223 change ($R^2 < 0.985$), or observations with stepwise concentration increases (interpreted as
224 ebullition) were omitted to ensure that the reported measurements represent purely diffusive
225 fluxes. Since ebullition was not measured from the hotspot monitoring chambers, our hotspot flux
226 estimates are conservative.

227 **2.5 Relating hotspot CH_4 fluxes to AVIRIS-NG observations**

Previous controlled release experiments determined the lower limit of AVIRIS-NG CH_4 flux detectability to be ~2 kg CH_4 hr^{-1} from point sources (Thorpe et al., 2016). While this flux rate is much higher than common CH_4 emission rates from northern wetlands, we expect AVIRIS-NG to be sensitive to significantly lower fluxes when air stagnation and the size of typical hotspots are taken into account. We developed a simple diffusion and advection plume model (Equation S3), to link ground-based observations with AVIRIS-NG observations and quantify the conditions necessary for AVIRIS-NG hotspot detection. We simulated diffusion rates based on typical in situ measurements in an artificial 10m x 10m hotspot from the Eastside Pond (5 x 5 grid of 2.1m pixels) to model expected AVIRIS-NG remote observations at various wind-controlled plume turnover rates. See Supporting Methods for a more detailed explanation. The maximum CH_4 enhancement observed at ground level (202 ppm CH_4) was then used in the hotspot simulation model to determine the effective wind speed and plume turnover time necessary to accumulate this CH_4 concentration given the prescribed hotspot flux rates.

2.6 ERT and NMR geophysical observations

In early September 2019, we conducted ground-based electrical resistivity tomography (ERT) geophysical surveys perpendicular to the north, east, and south shorelines of BTL, and collected borehole nuclear magnetic resonance (NMR) data adjacent to the north and east survey lines (James et al., 2020). Here, we focus on the eastern survey which transects the persistent Eastside Pond CH_4 hotspot. ERT images subsurface permafrost structure along 2D profiles to depths of 40 – 50 m by measuring spatial variations in electrical resistivity along a line of electrodes planted in the ground surface. Electrical resistivity is highly sensitive to the presence of liquid water, so thawed or wet zones exhibit vastly different values compared to dry or frozen soils (Briggs et al., 2017; Lewkowicz et al., 2016; Minsley et al., 2015, 2016). NMR was used to

observe total liquid water content and relative pore size distributions at 12.5 cm depth intervals from the surface to a depth of 2.1 m. NMR data were measured at a single location adjacent to the east ERT survey line, just inland on the eastern margin of the Eastside Pond. See Supporting Methods for a more detailed description of the ERT and NMR observation methods.

2.7 AVIRIS-NG surface classification for BTL CH_4 flux upscaling

The fraction of the CH_4 flux contributed by the Eastside Pond hotspot to the total CH_4 flux from the BTL environment remained a critical question. To address it, we analyzed the AVIRIS-NG reflectance imagery collected over a ~300m x 300m area centered on BTL and its surrounding nearshore environment. A spectral mixture analysis was generated using AVIRIS-NG reflectance imagery to apportion CH_4 fluxes to prominent surface types and represent hotspot fluxes in the context of study-area-wide emissions. A spectral library of prominent surfaces classes at BTL was developed based on a combination of expert-knowledge sub-sampling of BTL imagery and ground-based spectrometer surveys (ASD FieldSpec 4, ASD Products, Cambridge, UK) collected in July of 2019. Spectral endmembers were used in an iterative multiple endmember spectral mixture analysis (MESMA) (Roberts et al., 1998) to classify nine surfaces (open water, surface macrophytes (mostly *Potamogeton*), bare sediment, *Typha*, mixed wet grasses, dry grass + broadleaf, *Equisetum* dominant, mixed spruce, and senesced vegetation) within a 50 m perimeter surrounding the open water of BTL and the Eastside Pond, the boundary at which ground-based CH_4 flux observations extended from the shoreline. The resulting surface classification map was used to upscale CH_4 fluxes using chamber observations recorded in summers of 2018 and 2019 from corresponding surface types. Median fluxes for each surface type were multiplied by the area of each surface type within the domain to estimate total daily diffusive flux from BTL and its nearshore environment. Median flux from mixed wet grasses was applied to unclassified surfaces

274 (< 1% of total surface area) and senesced vegetation surfaces (3.1% of total surface area) since
275 chamber flux observations did not disambiguate these surface types, and because they typically
276 occurred within the mixed wet grass category at BTL. The mean of daily maximum flux rate (from
277 in situ closed chamber measurements) was used instead of the median for AVIRIS-NG-identified

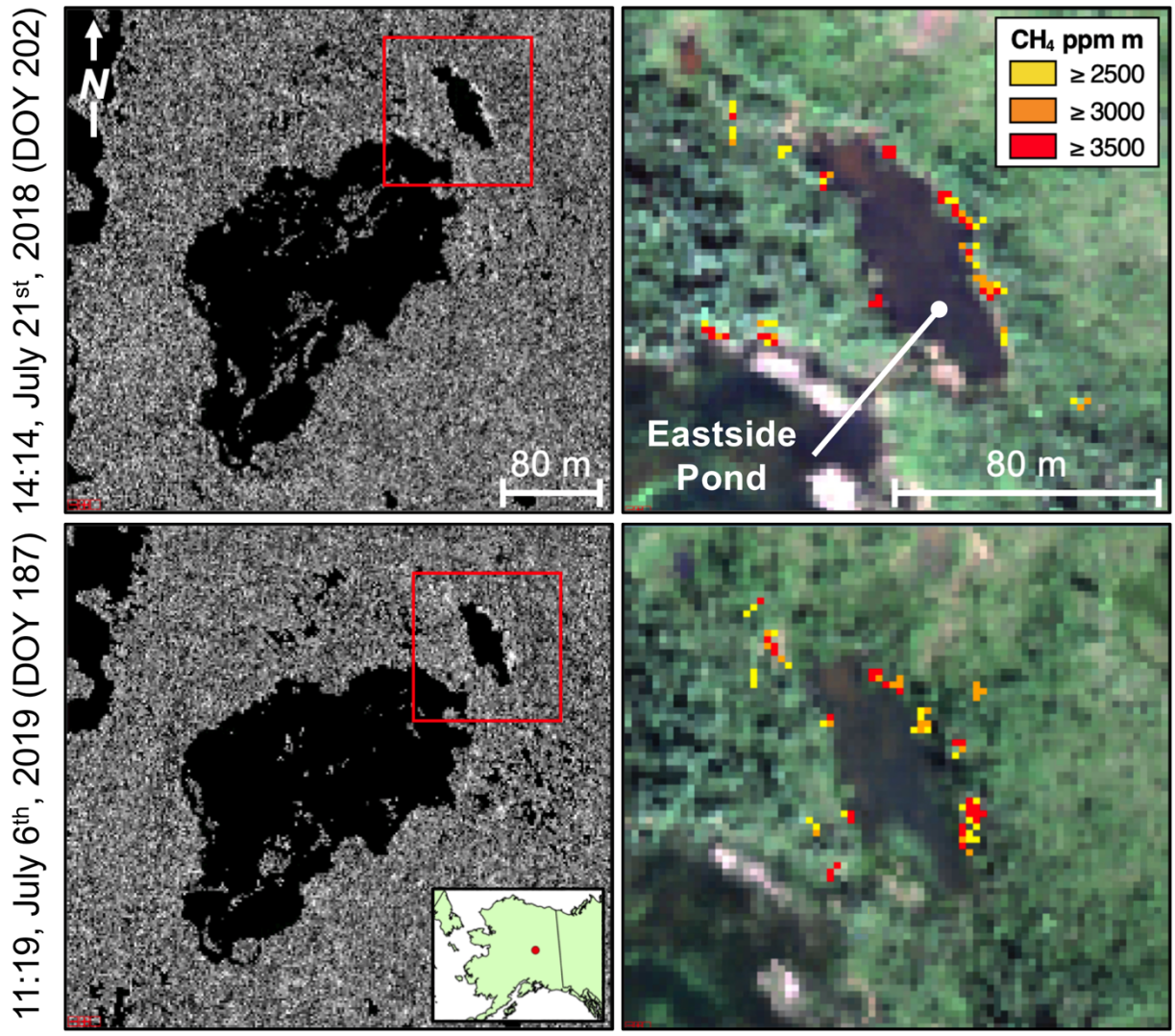

Figure 1. AVIRIS-NG remote detection of CH_4 hotspots at the Eastside Pond of Big Trail Lake (64.91932° N, -147.82200° W) in July 2018 (uppermost) and 2019 (lowermost). Times shown in AKDT. 2019 image taken two hours before ground-based survey shown in Figure 2. Greyscale panels (leftmost) show surface-controlled matched filter spectrometer output for column CH_4 enhancement. Rightmost panels show RGB channels overlaid with spectrometer output for spatially filtered CH_4 hotspots. Red outlines in the left images denote the extent of the RGB images. Local time of imagery is shown (AKDT).

hotspot surfaces only due to the variable nature of extreme CH_4 emission events within the chamber-flux dataset and the likely flux detection threshold of AVIRIS-NG.

3. Results

3.1 AVIRIS-NG remote hotspot detection

In multiple overflights during July 2018 and 2019, AVIRIS-NG detected persistent CH_4 hotspots concentrated on the north eastern margin of the Eastside Pond adjacent to the main body of BTL (Figure 1). While smaller more sporadic hotspots were also detected at other locations around BTL, the area shown in the inset/right panels of Figure 1 was the only region to consistently show significant CH_4 activity (Figure S3). Specifically, these NE margin hotspots were detected

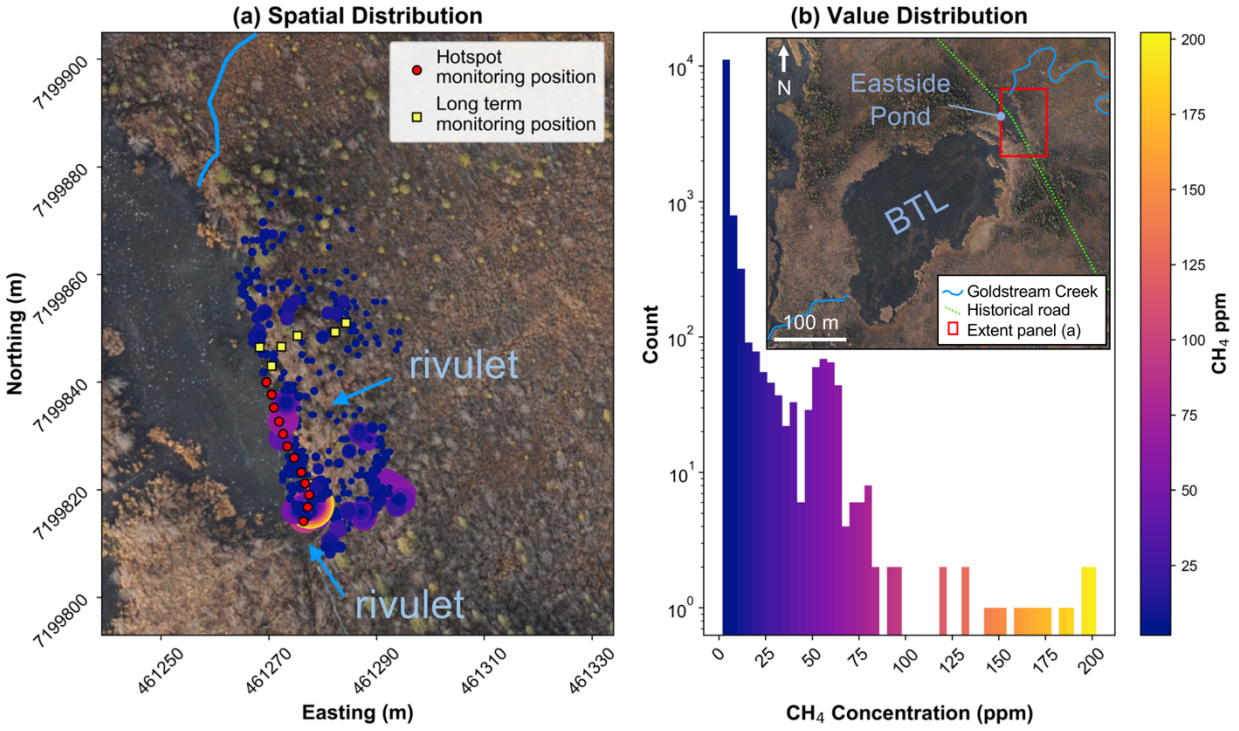

Figure 2. Ground-based CH_4 enhancement survey on July 6th, 2019 between 13:25 – 17:15 local time. Color scale in (a) and (b) correspond to CH_4 concentrations measured in ppm in air at ~0.5m AGL along a 10 cm/sec snaking transect that began in the SW and ended in the NE in panel (a) (see color bar for CH_4 scale). Gas concentration data was recorded at 1 hz. GPS position was updated every 30 sec. The size of the points in (a) are also scaled to their corresponding CH_4 ppm values. Individual points in (a) represent multiple gas concentration measurements but appear stacked due to lagged GPS updates. As a result, concentration data is accurate to ± 5 m. Red circles represent seasonal hotspot flux monitoring locations, whereas yellow squares represent long term flux monitoring with permanent chamber-collars (flux data not shown here).

in nine out of ten surveys flown ≤ 3,050 m AGL. Above this altitude, hotspots were only observed in two out of seven overflights. This is likely due to dilution of CH_4 enhancements over larger image pixels in higher altitude flights. Consistent with the findings of Elder, Thompson, et al. (2020), hotspots in general were more concentrated in the nearshore environment. The total hotspot area detected by AVIRIS-NG averaged 632 ± 460 m^2 within a 50-m-wide littoral perimeter around BTL and the adjacent thermokarst pond, or 0.62 ± 0.45% of the study area (i.e., lake + pond + terrestrial perimeter buffer).

3.2 Ground Based CH_4 observations

Remotely sensed hotspots detected at the Eastside Pond in the morning of 7/6/19 (Figure 1) were validated on the ground approximately two hours later on the same day (Figure 2). While most of the ground-based survey area resembled the area background CH_4 concentrations (~1.85 ppm), isolated regions with CH_4 concentrations up to 202 ppm were found near to the water's edge (Figure 2). These high concentrations were coincident in space with hotspots that were remotely sensed roughly two hours prior (Figures 1, and 2). Plumes of enhanced CH_4 (75 - 100 ppm) were detected several meters inland near the SE portion of the survey, corroborating occasional remote detections 10 – 20 m from the water's edge. Sporadic ebullition was also observed in the water column of the Eastside Pond during periods of the ground-based enhancement survey. It is possible that these emissions from the adjacent water surface (< 10 m away) influenced the ground-based enhancement survey, and potentially the remote hotspot detections; however, this effect was not quantified. Ebullition from the adjacent water column has no effect on closed chamber CH_4 flux observations (described in the next section). The peak enhancement of 202 ppm at 0.5 m AGL was applied in the hotspot plume diffusion and advection model to estimate the plume turnover time

necessary to produce these conditions at prescribed hotspot flux rates. The results are depicted in Figure S4, and discussed in Section 4.1.

Chamber-based CH_4 fluxes within the hotspot region were extreme (ranging up to 24,200 mg CH_4 m^{-2} d^{-1}), but also highly variable, spanning five orders of magnitude (Figure 3). Despite several extreme flux observations >2,000 mg CH_4 m^{-2} d^{-1}, hotspot-region fluxes often resembled high fluxes from other littoral zone locations at BTL (Figure S5) and the upper range of littoral zone mean fluxes reported in a pan-Arctic synthesis database compiled by Olefeldt et al. (2013) (Figure 3). Despite this variability, hotspot fluxes were significantly higher than non-hotspot fluxes at BTL ($p < 0.03$) when aggregating all observations from bare wet shoreline surfaces (including those observed outside the Eastside Pond hotspot region). Anomalous chamber-based fluxes from the Eastside Pond hotspot region extended into at least early winter 2019 and likely beyond, with an observed flux of 1,950 mg CH_4 m^{-2} d^{-1} on 12/14/19. This prolonged period of activity was

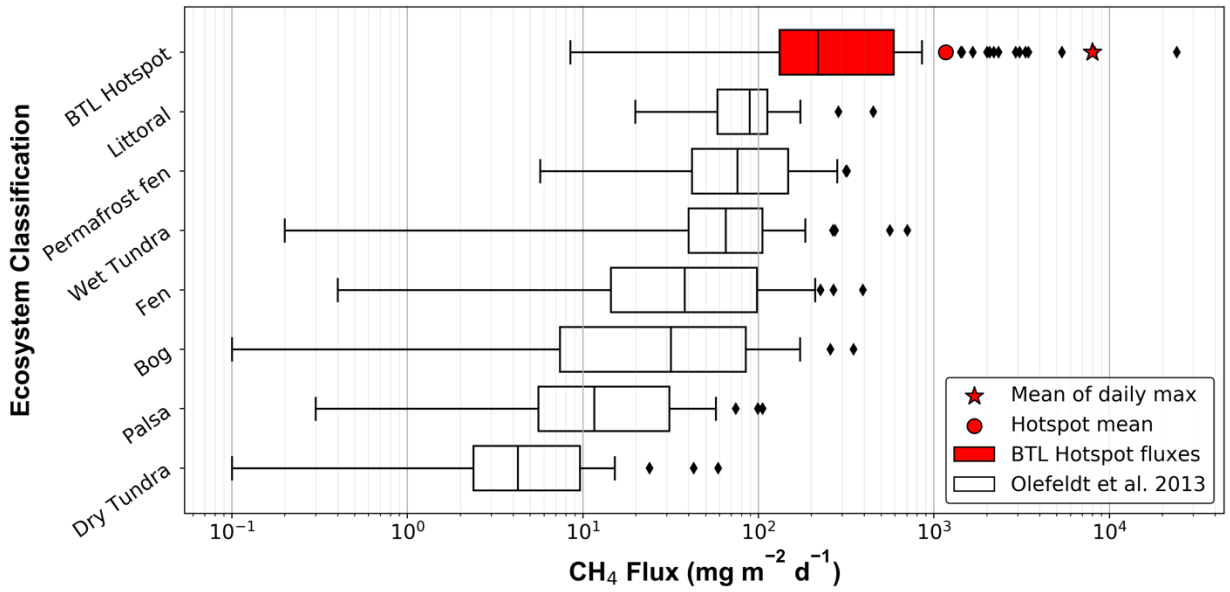

Figure 3. BTL CH_4 hotspot fluxes (n = 74) compared to distributions of site-level mean fluxes from various ecosystems in a pan-Arctic database. BTL hotspot fluxes were observed from 12 flux monitoring stations located within the remotely observed hotspot on 5 separate days between 7/7/19 and 9/17/19 (see Fig. S1). Database fluxes were taken from Olefeldt et al. (2013).

similar to the significant cold season fluxes observed from year-round studies of tundra CH_4 fluxes (Zona et al., 2015), and informed the 200-day timeframe used for estimating annual hotspot fluxes in our flux upscaling exercise discussed below.

3.3 Geophysical imaging of thermokarst features

Electrical Resistivity Tomography (ERT) inversion results produced a 2D cross-section through the NE margin of BTL and the Eastside Pond (Figure 4). Areas of low resistivity are interpreted as thawed and water-rich sediments, while areas of high resistivity indicate permafrost. Results revealed a prominent low-resistivity thaw bulb directly beneath the NE shoreline of the Eastside Pond to a depth of ~15 m, as well as an intermediate-resistivity undercutting partial thaw feature extending northeastward at depth. The shoreline thaw bulb coincided with the largest observed CH_4 fluxes and the remotely sensed hotspots. Fluxes decreased landward, where the ERT suggested the presence of an intact cap of permafrost between the active layer and the undercutting intermediate-resistivity feature, which may contain slightly elevated unfrozen water content.

In situ borehole NMR measurements of unfrozen water content with depth just inwards of the lake margin showed approximately 53% volumetric water content (VWC) within the 85 cm active layer (determined with manual frost probe), and residual 1-9 % VWC beneath the active layer to a depth of 2 m (Figure S6). These data showed there was significant unfrozen pore water in the low-resistivity active layer at this location, and that the shoreline thaw bulb at ~15 m depth, with similar low-resistivity vales, likely has comparable unfrozen water content available for microbial respiration of permafrost C.

3.4 Flux upscaling at Big Trail Lake

Spectral analysis of AVIRIS-NG imagery collected on July 5, 2019 mapped 9 unique surfaces and CH_4 hotspots across the terrestrial littoral zone of BTL. We used in situ data collected

in Elder, Thompson, et al. (2020) and during our 2019 field campaign to apportion flux values to each surface category (Figure 5). Diffusive fluxes from the 9 unique surface types, including their upscaled proportion of total study area fluxes are summarized in Supporting Table 1.

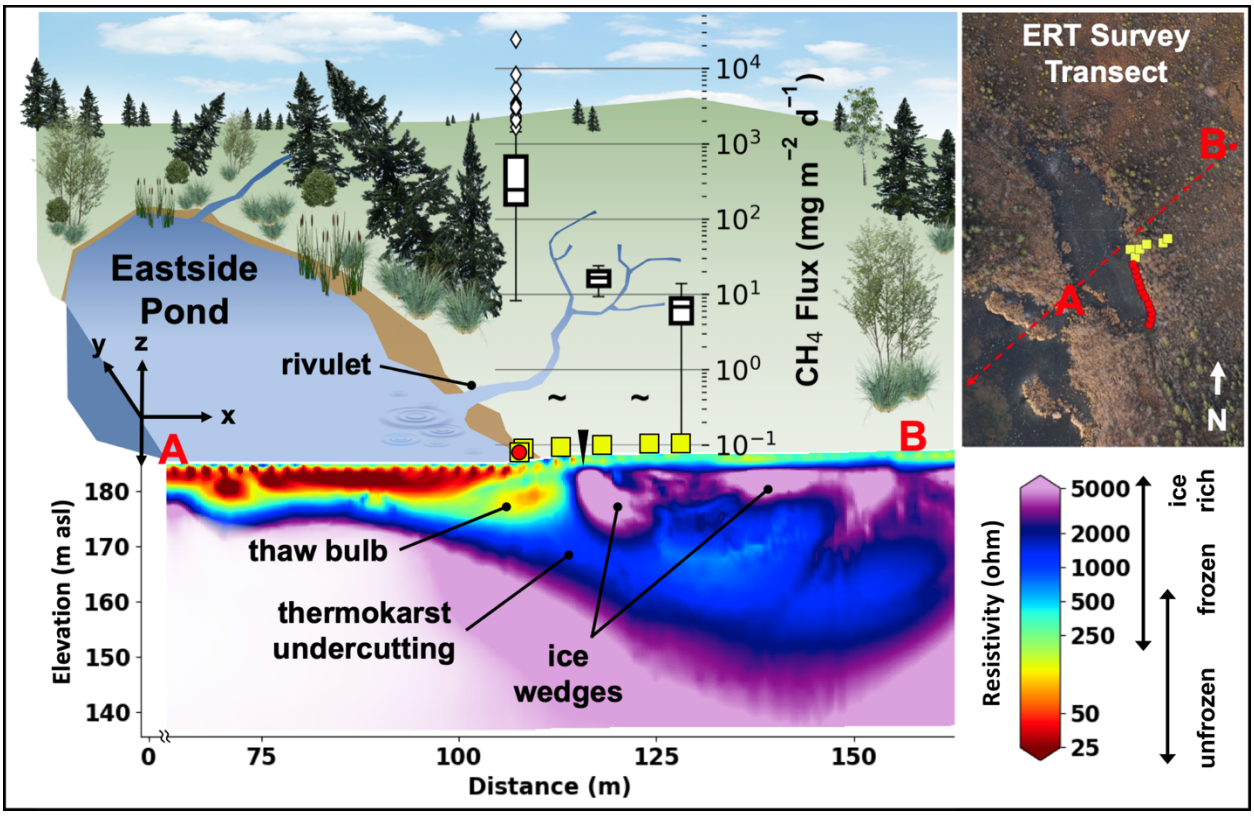

Figure 4. Electrical Resistivity Tomography (ERT) cross section identifies a thaw bulb beneath the easternmost shoreline of the Eastside Pond. Subsurface thermokarst features spatially align with extreme CH_4 fluxes from the remotely-sensed hotspot in the same area (white boxes). The red "A" and "B" correspond to the ERT transect extents in the x dimension. A black triangle marks the location of the NMR observation. The CH_4 flux graph represents data collected between 7/7/19 and 12/14/19. Flux data from two long-term monitoring positions (yellow squares) closest to shore were combined with data from the hotspot monitoring positions (red circles) in the first white box of the CH_4 boxplot. The "~" symbol represents negligible flux and all symbols are spatially accurate along the x dimension.

Hotspots comprised the largest proportion of study-area diffusive fluxes by a large margin (39.2%), with open water + macrophytes representing the next largest contribution at roughly 25% of total study area fluxes. Dry grasses + broadleaf surfaces were a small CH_4 sink; however, despite comprising 28% of the study area, only offset total study area fluxes by < 1%. In the July 5th AVIRIS-NG imagery, hotspots made up < 1% of BTL and its terrestrial littoral environment area, but represented roughly 40% of the total study area diffusive fluxes. Since remotely sensed

353 hotspots typically occurred near water, they mostly overlapped with wet sediment, *Typha*, and wet
354 mixed grass categories; however, this association is arbitrary since most wet sediment, *Typha*, and
355 mixed grasses areas were not hotspots at BTL. On rare occasions, hotspots were detected within
356 the dry grass + broadleaf and spruce surface types. The main factor we attribute hotspot emissions
357 to is enhanced thermokarst at the Eastside Pond, likely caused in part by water flow in multiple
358 rivulets that converge at the hotspot location. We estimate total daily diffusive fluxes (including
359 hotspot fluxes) from the 10.2 ha BTL study area (including lake body, Eastside Pond, and 50m
360 terrestrial buffer zone) to equal 13 kg CH_4 d^{-1} during the study period (July 2019). Including an
361 estimate of ebullition from BTL (293 mg CH_4 m^{-2} d^{-1}, (Engram et al., 2020; Walter Anthony et al.,
362 2018)), the total flux (diffusion + ebullition) from our study area is roughly doubled to 25 kg CH_4
363 d^{-1}.

364 To assess the relative flux associated with each surface type by proportional unit area, we
365 normalized surface fluxes by their proportional emission rate to the total, and then divided the
366 result by the proportional coverage of each surface. Table S1 shows the result. Hotspot areas
367 emitted significantly more CH_4 per proportional unit area than diffusive fluxes from all other
368 surface types at BTL (i.e., proportional flux > 65 times higher than its proportional area). This
369 supported the hypothesis that large proportions of thermokarst wetland fluxes can originate from
370 disproportionately small areas. The next most disproportionate surfaces were bare sediment (2.9
371 times), then *Typha* (2.4 times). Fluxes from wet mixed grasses were equal in proportion to their
372 area in the study domain (% flux : % area = 1.0), while Spruce, *Equisetum* dominant, and Dry
373 grass + Broadleaf surfaces were underrepresented in CH_4 flux per proportional unit area (≤ 0.5
374 times). If hotspot fluxes were not considered, flux proportions were 4.7 and 3.8 times greater than
375 the areal proportions for bare sediment and Typha, respectively. This implies that if explicit

hotspots, like those characterized here, go undetected in a hypothetical emissions survey, but another top-down method of calculating total area flux was used (i.e., eddy covariance), then fluxes from these surfaces could be over-estimated by a factor 1.5 – 2, leading to large discrepancies in upscaling efforts.

Table 1. Estimating annual pan-Arctic CH_4 hotspot fluxes attributable to thermokarst processes using estimates of mapped thermokarst, AVIRIS-NG hotspot metrics, and flux magnitudes observed on the ground from a persistent hotspot at the Eastside Pond.

Upscaling area description	Upscaling area (m^2)	Hotspot occurrence ratio (%)	CH_4 flux (mg m^{-2} d^{-1})	flux days^{-yr}	Pan-Arctic Hotspot Flux (g CH_4 yr^{-1})	% of total wetland flux > 45° N*
Very high lake and/or wetland thermokarst occurrence	$^{\delta}1.978 \times 10^{12}$	0.054^{Ψ}	1168[a]	200	2.5×10^{11}	0.8
			7984[b]		1.7×10^{12}	5.3
			24227[c]		5.2×10^{12}	16.2
Active lake and wetland thaw features	$^{\beta}1.498 \times 10^{11}$	0.243^{Φ}	1168[a]	200	8.5×10^{10}	0.3
			7984[b]		5.8×10^{11}	1.8
			24227[c]		1.8×10^{12}	5.5
Median					1.1×10^{12}	3.6

$^{\delta}$(Olefeldt et al. 2016), $^{\beta}$(Turetsky et al. 2020). $^{\Psi}$Area-weighted mean fraction from terrestrial surfaces in a 7,000 km^2 subset of ABoVE survey (see text). $^{\Phi}$Mean fraction within 45 m of open water bodies in Elder, Thompson, et al. (2020). [a]Mean of BTL hotspot flux data (n = 73). [b]Mean of daily maximum BTL hotspot fluxes (n = 5). [c]Maximum observed BTL hotspot flux (n = 1). *Annual Pan-Arctic flux of 32 Tg CH_4 yr^{-1} from Peltola et al. (2019).

4. Discussion

Hotspot fluxes observed at the Eastside Pond were extreme in the context of previously observed ecological emissions from northern terrestrial nearshore environments (Figure 3). Diffusive CH_4 fluxes reported in this study are among the highest measured from natural permafrost environments. This section discusses the magnitudes and spatiotemporal variability of the Eastside Pond hotspot flux observations and contextualizes them within the whole-ABoVE domain dataset of ~2 million AVIRIS-NG-detected hotspots. Additionally, our site-level flux validation, combined with the broad-area hotspot survey, forms a basis for estimating thermokarst CH_4 hotspot emissions on the pan-Arctic scale.

4.1 Extraordinary hotspot behavior

391 Elder, Thompson, et al. (2020) intensively surveyed CH_4 fluxes with chambers at 169
392 locations within the main lake body and on radial transects in the nearshore environment of BTL
393 in summer of 2018. Despite the intensive ground-based survey in July of 2018, the Eastside Pond
394 hotspot was not discovered until AVIRIS-NG hotspot maps of BTL were processed following the
395 2018 field campaign. During the 2019 field campaign, we created a fast data transfer protocol to
396 enable overnight processing of AVIRIS-NG output data and rapid production of CH_4 hotspot
397 maps. These maps were then used to guide in situ flux validation measurement surveys within 24-
398 48 hours of the 2019 AVIRIS-NG overflights.
399 Initial 2019 survey images (collected on 7/5/19) confirmed that the eastern margin of the
400 Eastside Pond was again the most active CH_4 region at BTL, as in 2018 (Figures 1, S3). Ground-
401 based CH_4 enhancement and flux validation at the Eastside Pond on 7/6/19 and confirmed CH_4
402 enhancements up to 202 ppm ~0.5 m above ground level at the Eastside Pond hotspot location two
403 hours after another AVIRIS-NG hotspot detection on 7/6/19 (Figures 1, 2).
404 Ground-based flux monitoring of the eastern margin of the Eastside Pond produced 74
405 diffusive CH_4 flux observations ranging from 8.5 to 24,000 mg CH_4 m^{-2} d^{-1} collected between
406 7/7/19 and 12/14/19. While AVIRIS-NG's mapping ability enabled precise geolocation (3-m
407 pixels) of the Eastside Pond hotspot in 9 out of 10 lower altitude flights, pinpointing the source of
408 this emission at any given time proved challenging using either our chamber flux monitoring array
409 or ground-based CH_4 enhancement survey. Our hotspot flux monitoring array, which was not
410 sampled continuously but sequentially on the day of observations, rarely captured the high
411 spatiotemporal variability of extreme hotspot fluxes within the confined (~3,000 m^2) area of the
412 eastern margin of the Eastside Pond. This further emphasizes the importance of high-resolution
413 remote sensing strategies for accurately tracking spatially and temporally sporadic extreme flux

events. The high variability of observed fluxes from the Eastside Pond hotspot region is apparent in Figure 3, where only the highest percentiles of observed fluxes are likely to result in detection by AVIRIS-NG. This variability presented a challenge for quantifying lower limit of AVIRIS-NG CH_4 hotspot detection.

To confirm whether the CH_4 fluxes from Eastside Pond could generate the 2500 - 3000 ppm m enhancement needed for confident AVIRIS-NG hotspot detection, we simulated the emissions with a plume diffusion and advection model and a flux of 8,000 mg CH_4 m^{-2} d^{-1}, equivalent to the mean daily maximum from our in-situ surveys. The model confirmed that this flux rate is detectable with 20 - 30 min of plume stagnation at the surface (Figure S4). If we used a flux of 24,000 mg CH_4 m^{-2} d^{-1}, corresponding to the maximum observed daily flux rate, the 2500 – 3000 ppm m enhancement threshold accumulated within 3 – 8 min (Figure S4). The same plume diffusion and advection model also determined that the maximum observed ground-based enhancement of 202 ppm CH_4 (at 0.5 m AGL) would require plume accumulation times of 6 min and 2.5 min at the mean of daily maximum and overall maximum observed flux rates, respectively. These results suggest that the flux which produced the hotspot that was detected in the ground-based enhancement survey (202 ppm CH_4 at 0.5 m AGL) and in multiple AVIRIS-NG overflights on 7/6/19 was likely closer to 24,000 mg CH_4 m^{-2} d^{-1} than to 8,000 mg CH_4 m^{-2} d^{-1} rate, and produced a plume that accumulated near the surface for roughly 10 min (Figure S4).

4.2 Characterizing and upscaling hotspot behavior at BTL

The localized concentrations of CH_4 hotspots in the terrestrial/littoral ecotone we discovered at BTL, and in AVIRIS-NG imagery from across the ABoVE domain, are consistent with the localized concentrations of ebullition hotspots observed in northern lakes (Walter Anthony & Anthony, 2013) and the shallow seas of the Arctic continental shelf (Thornton et al.,

2020). In each of these systems, a significant fraction of total CH_4 emissions originate from extreme fluxes occurring in a disproportionately small area. Similar to the spatial scarcity of lake ebullition and submerged permafrost CH_4 hotspots, terrestrial CH_4 hotspots were observed in only ~0.2% of the total 2017 AVIRIS-NG dataset and strongly concentrated near open water (Elder, Thompson, et al., 2020). While within lake ebullition can be detected visually (bubbling through water, or bubbles incased in winter lake ice), open water surfaces have a SWIR infrared reflectance of < 1% which effectively prevents AVIRIS-NG detection of CH_4 over water surfaces in our survey. This limits AVIRIS-NG's utility for observing within lake hotspots. However, the widespread detection of *invisible* terrestrial hotspot emissions near water in many ABoVE wetland

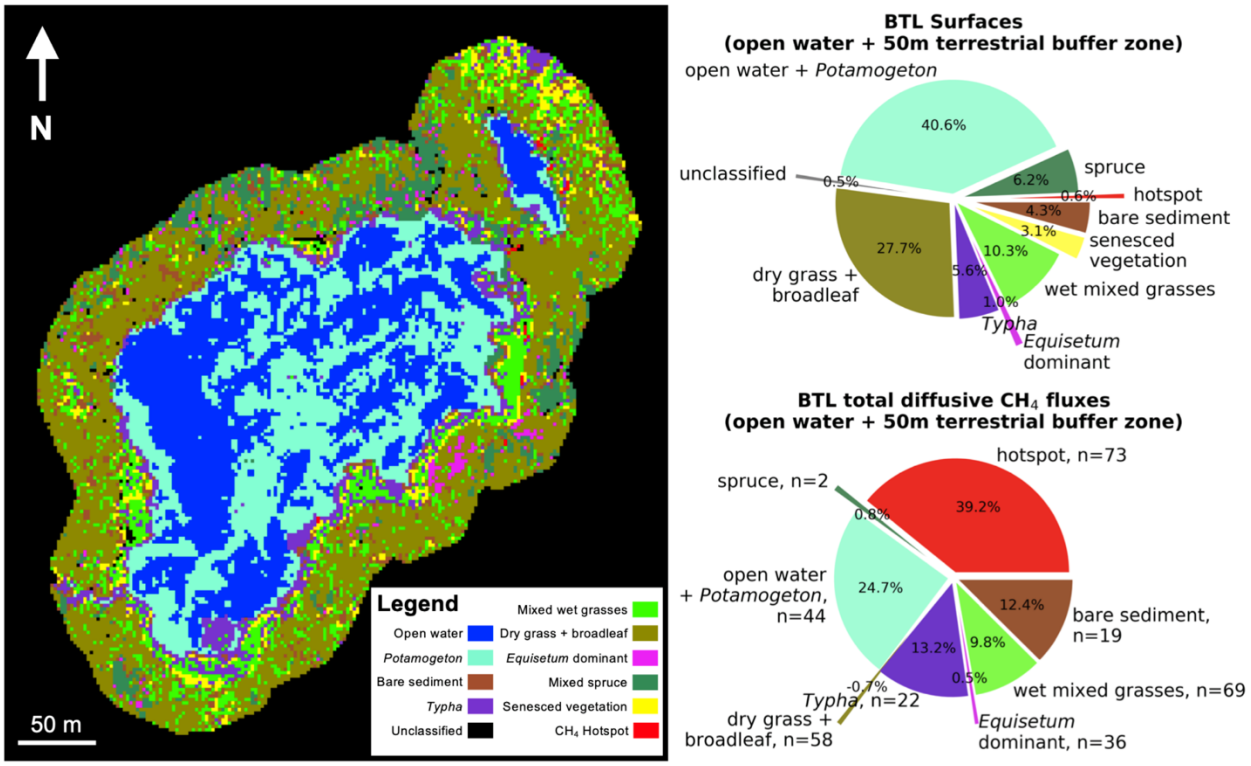

Figure 5. Diffusive CH_4 flux upscaling at BTL using 2018 and 2019 chamber flux measurements and AVIRIS-NG-based multiple endmember spectral mixture analysis (MESMA). Ebullition fluxes from the open water and *Potamogeton* areas are high (Walter Anthony et al., 2018), but are not considered in this analysis. The lake map was produced using an AVIRIS-NG reflectance image (2.1 m pixels) and CH_4 hotspot detection on July 5th, 2019 cropped to the study area. The median of chamber-based CH_4 fluxes was determined for each surface type and then multiplied by each surface's area within the map. Hotspots comprised less than 1% of the lake environment, but roughly 40% of the area's total diffusive flux.

regions is reshaping our understanding of where sites of intense thermokarst-related emissions can occur (Elder, Thompson, et al., 2020). We hypothesize that the same talik-related processes that drive intense, localized CH_4 ebullition within the margins of thermokarst water bodies also likely extend into the wet terrestrial nearshore environments, driving more elusive terrestrial hotspot CH_4 emissions.

The persistent CH_4 hotspots observed at the Eastside Pond were collocated with a ~15m deep talik and undercutting partial thaw feature that was identified using ERT measurements (Figure 4). Methane fluxes measured along the separate, permafrost-supported margin on the southern side of BTL, showed a more gradual decline moving away from water (Figure S7) compared with fluxes measured along the Eastside Pond transect which decline rapidly with distance from shore (Figure 4). For example, fluxes > 50 mg CH_4 m^{-2} d^{-1} were observed at distances greater than 20 m from the water's edge in the permafrost-supported southern margin of BTL but dropped to undetectable levels within 5 m of the Eastside Pond hotspot shoreline (Figure S7). In both cases, the magnitude of CH_4 flux was correlated with the thickness of thawed sediment identified from the ERT data. However, the AVIRIS-NG hotspots and extreme chamber fluxes were only observed proximal to the thermokarst features of the Eastside Pond margin where the thawed depth may extend beyond 15 m (~5 m deeper than on BTL's southern margin) (Figures 4, and S7). Although both the Eastside Pond and southern margin of BTL show relatively deep thaw, more recent thermokarst expansion in the Eastside Pond, compared with the older, stable, permafrost-supported southern margin of BTL, may contribute to this difference given greater availability of more recently thawed permafrost C (Walter Anthony et al., 2018). Differences in thaw age and extent are also supported by the intermediate resistivity values observed in the

468 Eastside Pond talik, indicating partially thawed/frozen sediments, compared with uniformly low
469 resistivity on the southern side of BTL -representative of fully thawed sediments (Figure S7).
470 It is likely that the Eastside Pond shoreline talik is contributing to the anomalous CH_4 fluxes
471 either by supporting enhanced microbial activity within the saturated and partially thawed shallow
472 sediments, and/or by serving as a pathway connecting water and gases with deeper permafrost C.
473 The latter may represent a preferential flow path for deeper CH_4 to reach the atmosphere, similar
474 to hypothesized patterns within lake taliks (Walter et al., 2008), by allowing CH_4 to diffuse or
475 advect in thawed channels past the near-surface intact ice wedges and towards the thawed margin
476 at the pond's shoreline. This in effect may concentrate CH_4 from a larger subsurface methanogenic
477 volume into a relatively small area of intense, AVIRIS-NG-detectable emissions at the surface.
478 Although we indirectly link potential talik CH_4 production and potential deep CH_4 channeling via
479 liquid water in the undercutting feature to extreme CH_4 flux at the terrestrial surface, collocation
480 of these prominent thermokarst features at the remotely-sensed CH_4 hotspot support our central
481 hypothesis that these mechanisms promote spatially intensive hotspots of CH_4 release to the
482 atmosphere. Ongoing work will utilize isotopic techniques to further investigate the sources of the
483 Eastside Pond CH_4 hotspot and explore broader emergent relationships between thermokarst and
484 CH_4 hotspots in the domain-wide CH4 hotspot dataset.
485 To contextualize observed CH_4 hotspot emissions within total CH_4 emissions from the
486 BTL environment, we developed a MESMA-based land surface classification using AVIRIS-NG
487 and ground-based spectral data of the study area to upscale surface-type-specific fluxes across the
488 study area (Figure 5). A powerful aspect of the AVIRIS-NG data is that this classification uses the
489 same exact imagery as the CH_4 hotspot product, resulting in perfect collocation of the CH_4 hotspot
490 and surface classification products. Median CH_4 fluxes from the in situ chamber measurements

were assigned to individual land cover types, and then the total CH_4 flux from the BTL environment was estimated. This analysis revealed that the hotspot fluxes comprised 40% of the total diffusive CH_4 fluxes from the study area, but that hotspots accounted for only 0.6% of the land area in the BTL domain. This underscores the disproportionate importance of relatively fine-scale ecological/geomorphological dynamics, even within similar surface types, in site-to-landscape scale CH_4 emission upscaling and budgeting. While our MESMA classification only covered BTL and a 50-m terrestrial buffer zone around its perimeter, it demonstrates the value in high resolution imagery for accurately upscaling CH_4 fluxes across heterogeneous environments. Future classifications will exploit full-scene AVIRIS-NG spectral data to produce landscape-scale CH_4 flux attribution maps.

4.3 Upscaling thermokarst CH_4 hotspot emissions to the pan-Arctic

To determine the likelihood of hotspot occurrence in thermokarst environments beyond BTL, we analyzed a subset of 65 AVIRIS-NG flight lines from 2017, 2018, and 2019, shown in red in the upper panel of Figure 6, that surveyed ~7000 km^2 spanning variable wetlands, lake types, and levels of thermokarst occurrence as classified by Olefeldt et al. (2016). For simplicity, only areas classified as having either “very high” wetland and/or lake thermokarst occurrence or “low” wetland and/or lake thermokarst occurrence were identified in this analysis and all intermediate thermokarst categories were grouped. Hillslope-type thermokarst regions were not considered since they are least likely to collect water and produce the anaerobic conditions needed for high CH_4 production. We assume the 7,000 km^2 subset of AVIRIS-NG flight lines, which sub-samples the majority of the spatial extent of the ABoVE study domain, is spatially representative of diverse lake and wetland types found throughout the pan-Arctic. We found that hotspots were up to 2.5 times more likely in wetland and/or lake areas classified as very high thermokarst occurrence

versus wetland and/or lake areas with low thermokarst occurrence (lower panel of Figure 6). This further supports our hypothesis that thermokarst and/or abrupt thaw features promoted the extreme, spatially localized CH_4 emissions observed by AVIRIS-NG. The flight line-weighted hotspot occurrence ratio from "very high" thermokarst occurrence areas (total hotspot area/total terrestrial area = 0.00054) was determined as the basis for estimating total thermokarst hotspot area across the pan-Arctic.

Combining spatial thermokarst occurrence statistics with our field measurements at the Eastside Pond hotspots, we estimated annual pan-Arctic CH_4 emissions from thermokarst hotspots. We estimated the total area that was similar in character to the Eastside Pond hotspot using two different methods. The first approach extrapolated the AVIRIS-NG-observed hotspot thermokarst hotspot occurrence ratio (0.054%) over all Arctic terrain likely to contain very high rates of thermokarst occurrence. Since the AVIRIS-NG CH_4 survey only measured land surfaces, we subtracted open water thaw lake area (280,000 km^2, (Turetsky et al., 2020)) from the total pan-Arctic mapped area classified as "very high" in either or both of the thermokarst lake or thermokarst wetland categories in Olefeldt et al. (2016). This produced a pan-Arctic terrestrial upscaling area of 1,978,000 km^2. We multiplied this area by the AVIRIS-NG based hotspot area fraction of 0.00054 to estimate total thermokarst CH_4 hotspot area in pan-Arctic regions of very high thermokarst occurrence. Our second approach extrapolated hotspot activity based on discrete areas of current active/abrupt thaw features (i.e., not inclusive of broader areas where they are likely to occur as in Olefedt et al. (2016)). Here we added the area of currently active abrupt lake thermokarst (78,100 km^2, pers. comm. M. Turetsky) to the area of currently active organic lowland wetland thermokarst (71,700 km^2, pers. comm. M. Turetsky). This area represents features which were likely to occur near the presence of water and thus fall within the study domain of Elder,

537 Thompson, et al. (2020), which determined hotspot Poisson rates with respect to distance from the
538 nearest water body up to 250 m. We multiplied this discrete active/abrupt thaw area by a higher
539 hotspot occurrence ratio (0.243%) based on the integrated CH_4 hotspot Poisson rate within 45 m
540 of water surfaces, a critical distance threshold in the 30,000 km^2 2017 AVIRIS-NG AAC (Elder,
541 Thompson, et al., 2020). This estimated hotspot proportionality within discrete active/abrupt areas
542 as described in Turetsky et al. (2020). This hotspot fractional area (0.243%) was conservative since
543 it was originally determined with respect to waterbodies in both thermokarst and non-thermokarst
544 areas, where we expect the latter to have fewer hotspots.

545 We then extrapolated ground-based hotspot flux measurements from the Eastside Pond and
546 the remote hotspot occurrence areas, described above, to estimate pan-Arctic CH_4 fluxes
547 attributable to thermokarst processes. We used the Eastside Pond hotspot overall mean CH_4 flux
548 (n = 74), the mean of daily CH_4 flux maximum (n = 5), and maximum CH_4 flux measured from all
549 74 observations. The median value of observed hotspot fluxes (218 mg CH_4 m^{-2} d^{-1}) was excluded
550 in upscaling since it was unlikely to produce the CH_4 enhancements observed at ground level
551 (Figure 2) nor the lower hotspot detection threshold of AVIRIS-NG for this study (≥ 2500 – 3000
552 ppm m CH_4) (Equation S3, Figure S4). This lower detection threshold is more probable at flux
553 rates comparable or greater than the observed mean of daily maximum fluxes from the Eastside
554 Pond hotspot (~8000 mg CH_4 m^{-2} d^{-1}). Since anomalous Eastside Pond hotspot fluxes were
555 observed until at least 12/14/19, and recent year round measurements suggest cold season
556 permafrost-region CH_4 fluxes could outweigh growing season fluxes (Zona et al., 2015), each daily
557 flux rate was multiplied by 200 days to estimate annual hotspot fluxes. These fluxes, were then
558 multiplied by either the discrete area of pan-Arctic thermokarst features (1.498×10^{11} m^2) and their
559 respective hotspot occurrence ratio (0.243%), or pan-Arctic areas with very high likelihood of lake

and/or wetland thermokarst occurrence (1.978 x10^{12} m^2) and their adjusted hotspot ratio (0.054%) to obtain a range of annual pan-Arctic CH_4 hotspot fluxes attributable to thermokarst (Table 1).

Using these two approaches, we estimate that current thermokarst CH_4 hotspot emissions comprise 1.1 Tg CH_4 (range: 0.1 – 5.2 Tg), or roughly 3.6% (0.3 – 16.2%), of annual pan-Arctic wetland CH_4 emissions (Table 1). This flux originates from a total hotspot area of ~720 km^2 or roughly 0.005% of the high latitude permafrost region- a resulting disproportionality ~700 times the proportional flux per proportional area (i.e., % hotspot flux of total : % hotspot area of high latitude permafrost area). This calculation is summarized in Table 1. This pan-Arctic hotspot flux disproportionality factor (~700) is an order of magnitude greater than the factor of ~65 determined from our MESMA-and flux-chamber-based emissions upscaling of the local BTL environment. This demonstrates that thermokarst CH_4 emission hotspots act as islands of exponentially disproportionate CH_4 emissions on spatial scales that expand beyond lake and proximal wetland environments.

4.4 Caveats to upscaling pan-Arctic hotspot fluxes

Detectability of CH_4 hotspot fluxes by AVIRIS-NG is primarily a function of flux magnitude and wind speed (or plume stagnation), where higher wind speeds diminish CH_4 enhancement and detectability. Alternatively, lower fluxes may be detectable where surface roughness, caused by standing vegetation or microtopography (common in the permafrost domain), result in near-surface air stagnation and CH_4 accumulation over longer periods. Despite the high spatiotemporal variability of these factors across the high northern latitudes, our diffusion and advection plume model (Figure S4) showed that the flux rates observed from the Eastside Pond margin (5,000 – 24,000 mg CH_4 m^{-2} d^{-1}) and plausible plume turnover (stagnation) times of 5-20 minutes lead to hotspots that could be detected by AVIRIS-NG. These conditions are

583 consistent the very low wind conditions common at BTL during the clear-sky summer days when
584 AVIRIS-NG typically acquired imagery. These low-wind conditions, which were confirmed by
585 wind observations at the eddy covariance tower on BTL (commonly < 1.5 m/s during overflights),
586 are characteristic of potential "clear sky bias" weather conditions which apply to all AVIRIS-NG
587 scenes. This bias could increase the sensitivity of AVIRIS-NG to lower flux rates if low windspeed
588 and greater air stagnation, particularly in sheltered environments, allowed enhancements to
589 accumulate to higher concentrations at ground level. As a result, upscaled pan-Arctic thermokarst
590 fluxes based on our BTL observations, may be overestimated. However, this effect is likely more
591 than counterbalanced by two other aspects of the survey which render our pan-Arctic emission
592 estimate more conservative. Firstly, the Eastside Pond hotspot was only detected in 30% of higher-
593 altitude AVIRIS-NG flights (> 3,050 m AGL), which is more representative of the ~5,000 m AGL
594 altitude in the broader ABoVE surveys. Thus, hotspots with the flux magnitude similar to that of
595 the Eastside Pond hotspot were more often undetected in the broader survey. This would
596 effectively reduce the total number of detected hotspots and reduce our pan-Arctic hotspot
597 emissions estimate. Secondly, AVIRIS-NG is not sensitive to CH_4 enhancements over water
598 surfaces due to their low reflectivity in the SWIR infrared wavelengths used for the CH_4 retrieval.
599 Thus, AVIRIS-NG does not capture complete thermokarst flux variability in space, time, and
600 magnitude, especially in regions with one-off or infrequent overflights. This would further reduce
601 the frequency of hotspots in our survey and our upscaled hotspot emissions estimate.
602 Since ebullition was frequently observed in the water < 10m (and downwind) from the
603 AVIRIS-NG detected hotspots at the Eastside Pond, it is possible that these water-borne emissions
604 occasionally combined with detectable fluxes observed from the adjacent SWIR-reflective land
605 surface and/or nearby plant-mediated fluxes to promote local CH_4 enhancements to the lower

606 AVIRIS-NG detection limit. If this effect is widespread in the ABoVE AVIRIS-NG surveys, it
607 means our surveys remain sensitive to regions where ebullition is strong enough and close enough
608 to land (typical of lake thermokarst margins) to be detected. This would also likely lead to an
609 underestimation of the spatial extent and flux rates necessary to render such an enhancement. This
610 effect, combined with the inability to observe lower-level water fluxes with plumes that do not
611 extend over land, or higher fluxes further from the SWIR-reflective surfaces of land, further
612 supports the conservatism of our pan-Arctic upscaling.

613 We did not quantify these effects, but we believe this variability is captured in our estimated
614 range of annual CH_4 flux from thermokarst features (0.1 - 5.2 Tg CH_4 yr^{-1}). Despite this wide
615 range, our two independent approaches overlap between 0.3 – 1.8 Tg CH_4 yr^{-1} (median across all
616 estimates = 1.1 Tg CH_4 yr^{-1}, Table 1). Although this estimate carries relatively large uncertainty,
617 it is conservative and it exploits our novel CH_4 hotspot survey, which spans spatial scales from
618 25m^2 to 70,000 km^2, and represents a unique observation-based apportionment of CH_4 fluxes to
619 complex and climate-sensitive thermokarst processes. This estimate could serve both as an
620 important baseline for monitoring future CH_4 emissions from accelerating permafrost thaw, and a
621 tool to potentially allocate thermokarst emissions in top-down and bottom-up emission accounting
622 and projections.

623 Aside from ground-based determination of flux magnitudes required to produce an
624 AVIRIS-NG CH_4 hotspot, our approaches to upscaling CH_4 fluxes to pan-Arctic thermokarst
625 processes leveraged the ability of AVIRIS-NG to determine hotspot areal coverage relative to total
626 imaged area (hotspot occurrence ratio) at very high spatial resolution (25 m^2 pixels) over more
627 than nine orders of magnitude (nearly 100,000 km^2 imaged through 2019). Despite this
628 unprecedented sampling across spatial scales, direct determination of total hotspot area was not

629 possible. Thus, our approaches rely on two key assumptions. Firstly, all hotspot areas, despite
630 quantitative AVIRIS-NG CH_4 enhancement variability, were assigned the same flux value in each
631 respective upscaling approach. This equates to the assumption that the flux values observed at the
632 Eastside Pond are representative of hotspot fluxes across the Arctic. Secondly, we assume that
633 thermokarst produces all hotspot emissions within the upscaling regions defined by our two
634 approaches.

635 Our two approaches therefore differ in the way that they estimate the total area of Arctic
636 thermokarst features. The first approach, estimates the fraction of thermokarst within the entire
637 mapped area of very high wetland and/or thermokarst occurrence determined by Olefeldt et al.
638 (2016), while the second method directly estimates discrete areas of thermokarst features (M.
639 Turetsky, pers. comm.). The first approach likely overestimates the area corresponding to
640 thermokarst-driven hotspots; however, we expect this overestimation to be counterbalanced by the
641 likelihood that the second approach underestimates hotspot occurrence- since the hotspot
642 occurrence ratio we applied was determined in large part from areas without thermokarst features.
643 For example, hotspots in the BTL study area (representing a young/active thermokarst
644 environment) occurred in 0.62 ± 0.45% of the study area, while the hotspot fractional area used
645 for discrete pan-Arctic thermokarst features was almost three times less (0.243%, Table 1).
646 Nevertheless, we believe that the median pan-Arctic flux estimate of 1.1 Tg CH_4 yr^{-1} from all of
647 our upscaling approaches is conservative since it falls in the range where our estimates overlap.

648 It is likely that the mechanisms that regulate episodic ebullition events within the water
649 columns of lakes also exist in the adjacent nearshore terrestrial environment. However, a key
650 difference is that these pulse-like emissions in the saturated, but not inundated, near-shore
651 environment likely more closely resemble periodically high rates of diffusion instead of the abrupt

652 emissions characteristic of ebullition events in water. As discussed in Windsor et al. (1992), it is
653 possible that episodic ebullition-like releases of CH_4, originating from deeper, saturated sediments,
654 are transformed by the overlying soil/sediment matrix along waterbody margins into more diffuse
655 emission modes. This effect is clear when comparing closed chamber observations of ebullition
656 flux, where chamber CH_4 concentrations exhibit stepwise increases during ebullition, with the
657 consistent (linear) concentration increase of pure diffusion. Indeed, our observed extreme diffusion
658 rates (mean: 1,110 mg CH_4 m^{-2} d^{-1}, n = 74) closely resemble high ebullition-flux rates previously
659 observed from young/active yedoma thermokarst lakes in Siberia and Alaska (Sepulveda-Jauregui
660 et al., 2015; Walter Anthony et al., 2010, 2016). Although rapid, non-linear concentration increases
661 were occasionally observed within the hotspot monitoring chambers, these measurements were
662 discarded due to the potential that even small chamber agitations during measurement could trigger
663 ebullition events in the sensitive sediments. Considering this, our measurements of extreme
664 hotspot flux rates only represent consistent diffusion rates, and thus could underestimate total
665 hotspot flux if ebullition-like events also occur in the terrestrial sediments of the nearshore
666 environment. However, in the context of our upscaling of surface-specific fluxes at BTL (Figure
667 5), ebullition was not considered, meaning a significant fraction of CH_4 flux (via ebullition from
668 open water at BTL) was not included in the study area proportional flux analysis. In a separate
669 analysis, BTL ebullition flux is estimated to equal 293 mg CH_4 m^{-2} d^{-1} (Engram et al., 2020; Walter
670 Anthony et al., 2018). If this flux is considered in addition total diffusive fluxes, then the proportion
671 of CH_4 flux from AVIRIS-NG hotspots would decrease from ~40% to ~20% of total BTL
672 environment emissions and open water surfaces would overtake hotspots as the greatest
673 contributor to study area CH_4 flux (~60%) (albeit from an area 40 times larger).
674

675 **4.5 Origins of CH_4 hotspots**

676 On the surface above the Eastside Pond talik, several small rivulet streams each created 1
677 – 2 m deep depressions, elongated 3 - 6 m to the east and perpendicular to the main axis of the
678 Eastside pond. The rivulets with more consistent water flow appeared to spatially correlate with
679 high fluxes, detected hotspots, and ERT-observed subsurface thermokarst features. These
680 depressions may reflect voids that were previously occupied by massive ice wedges, like those
681 observed subsurface and to the east of the Eastside Pond in the ERT cross-section (Figure 4). The
682 degradation of ice wedges likely accelerates thermokarst at the Eastside Pond and promotes
683 enhanced mineralization of permafrost C to CH_4 in the subsurface. Furthermore, the surface
684 depressions are somewhat sheltered from ventilation, creating ideal conditions for air stagnation
685 and CH_4 accumulation near the surface. Hydrophytic vegetation is also abundant on the margins
686 of the Eastside Pond and may combine with supplemental permafrost-C-sourced CH_4 to elevate
687 emissions through vascular plant tissues (Andresen et al., 2017; Ström et al., 2003).

688 Further characterization of the origins of remotely-detected CH_4 hotspots would greatly
689 benefit from isotopic analysis ($\Delta^{14}C$, $\delta^{13}C$, δD, clumped isotopes) of the emitted gas. Such analysis
690 would improve apportionment of hotspot fluxes potentially originating both ancient permafrost C
691 or from sub-permafrost, geologic C sources (Douglas et al., 2020; Walter Anthony et al., 2012).
692 However, given the 2 million CH_4 hotspots detected by AVIRIS-NG across the surveyed area of
693 the ABoVE domain (Elder, Thompson, et al., 2020), ecologic C sources (permafrost C and/or
694 actively cycling surface C) likely dominate hotspot emission sources. In future studies, the
695 AVIRIS-NG CH_4 survey could be a valuable tool to guide more intensive ground-based isotopic
696 investigations towards sites of extraordinary CH_4 emissions.
697

698

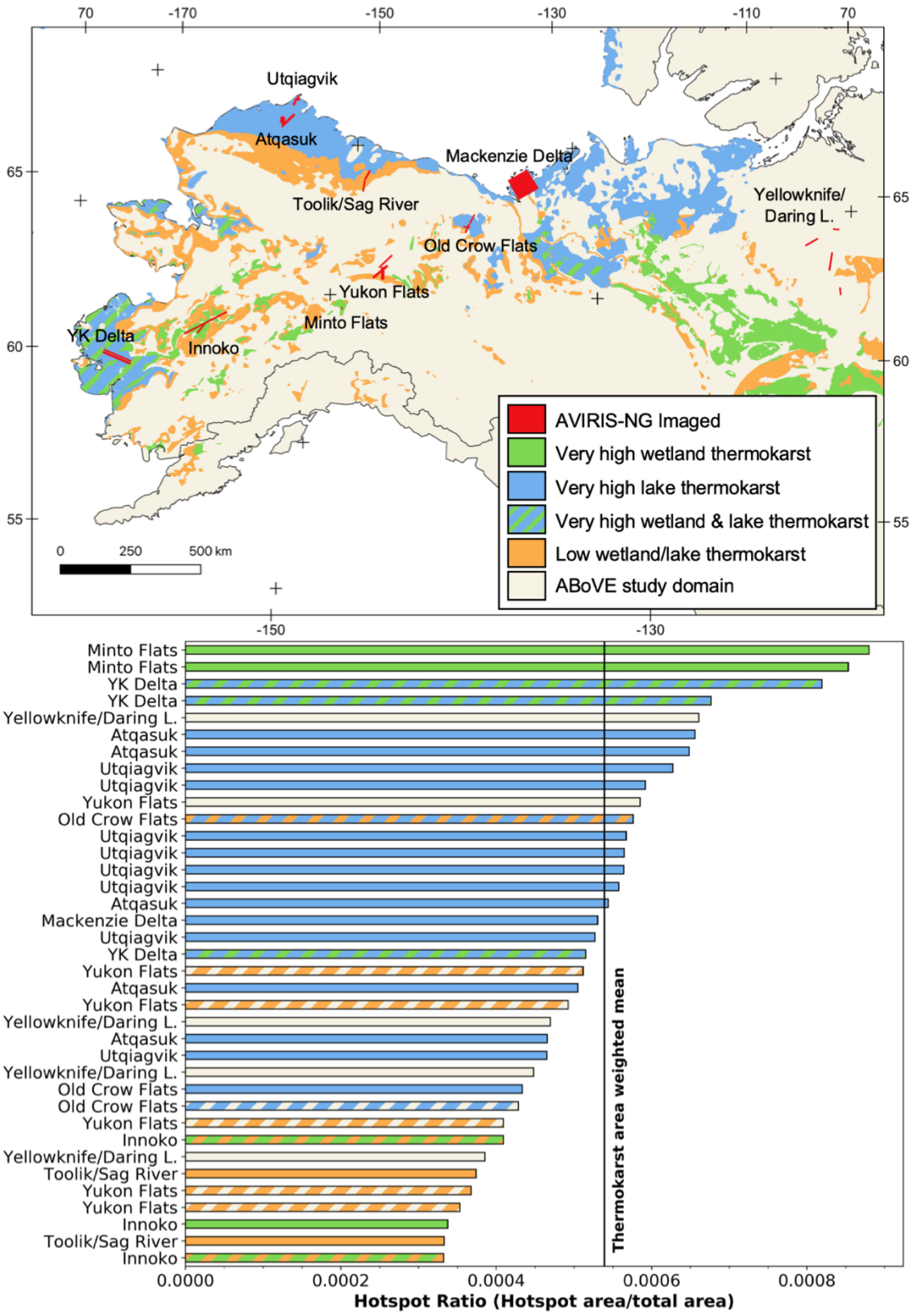

Figure 6. Hotspot ratios by region. Upper panel: subset of 65 AVIRIS-NG flight lines from 2017 -2019 mapped in relation to either "very high" or "low" thermokarst characteristics classified by Olefeldt et al. (2016). Intermediate thermokarst values were not characterized. Lower panel: AVIRIS-NG-based CH_4 hotspot occurrence ratio ranked for each flight line (Mackenzie Delta mosaic plotted as a single bar). Bars are color-coded based on map legend.

4.6 Regional CH_4 hotspot patterns

While it is difficult to determine whether thermokarst features like those at BTL are the predominant driver of CH_4 hotspot occurrence in the broader AVIRIS-NG survey, we suspect this to be the case given the increased likelihood of hotspot occurrence in very high vs. low thermokarst environments (Figure 6). Our observations of high CH_4 hotspot activity, particularly in the Yukon Kuskokwim Delta and Alaskan North Slope (Figure 6), correspond to elevated CH_4 emissions in the same regions as determined from inverse modelling of airborne concentration data (S. M. Miller et al., 2016). This suggests that CH_4 hotspots may be the dominant mode of CH_4 emission in regions that are conducive to thermokarst. While outside the scope of this study, future work will focus on more quantitative comparisons between AVIRIS-NG hotspot patterns and other complimentary airborne (Kohnert et al., 2018; Miller et al., 2016; Sweeney et al., 2020) and spaceborne CH_4 remote sensing observations (Engram et al., 2020).

The Innoko wetlands proved an exception to the patterns shown in Figure 6. Reasons for the low hotspot occurrence in the Innoko wetlands are unexplained, especially since high fluxes are expected from this peaty-silty lowland region riddled with collapse-scar bogs and fens (Jorgenson et al., 2013). The observation could relate to lower densities of AVIRIS-NG-detectable extreme emission sites which were more characteristic of yedoma or lake thermokarst regions. Innoko CH_4 hotspot activity may have also been suppressed by local environmental/meteorological conditions on the day of observation.

4.7 Implications for current and future pan-Arctic CH_4 emissions

While our best estimate of CH_4 flux from pan-Arctic thermokarst is only around 4% (1.1 Tg CH_4 yr^{-1}) of total estimated pan-Arctic wetland emissions (32 Tg CH_4 yr^{-1}, sans lake emissions (Peltola et al., 2019)), it may represent a previously unaccounted source within pan-Arctic

emission budgeting. Given the high uncertainty range of our estimate (range 0.1 – 5.2 Tg CH_4 yr^{-1}), thermokarst may be responsible for substantially more than (or less than) 1.1 Tg CH_4 emissions annually. Our observed hotspot fluxes are amongst the highest natural CH_4 fluxes reported in the literature (Olefeldt et al., 2013). We believe that the hotspot emissions represented here, and particularly their widespread occurrence, have until now gone mostly unobserved and undescribed. Without the ability to observe extreme *terrestrial* flux events at high spatial resolution and broad coverage, and with limited datasets of high-spatial-resolution CH_4 flux observations (i.e., spatially confined chamber fluxes) from thermokarst environments, such events likely went undetected prior to the AVIRIS-NG survey. However, it's also safe to assume that not all thermokarst environments are capable of emitting CH_4 at high enough rates to meet the AVIRIS-NG hotspot threshold definition (likely 5 – 15 g CH_4 m^{-2} d^{-1} given probable plume turnover times). If hotspots, like those characterized here, were undetected and unaccounted in previous research, our estimate would, in effect, increase bottom-up flux estimates and widen their discrepancy with top-down emission accounting. For example, Walter Anthony et al. (2016) estimates emissions of 2.2 – 6.7 Tg CH_4 yr^{-1} from thermokarst lake margin expansion during the last 60 years. However, this estimate does not include hotspot fluxes from the nearshore terrestrial environment, a buffer zone extending from the water's edge where Elder, Thompson, et al. (2020) showed that hotspots are most likely to occur within 45 m of the shoreline. Our results suggest that the 2.2 – 6.7 Tg CH_4 yr^{-1} estimate from lake thermokarst expansion zones could be underestimated by 25 – 50% since nearshore terrestrial hotspots were not considered.

Bottom-up accounting typically estimates double the pan-Arctic emissions of top-down methods (59.7 (36.9 – 89.4) vs. 23 ± 5 Tg CH_4 yr^{-1}, respectively, including lake flux (Thornton et al., 2016)). Given the high uncertainty in both accounting approaches, it is plausible that terrestrial

745 thermokarst CH_4 hotspots account for a "newly known" emission mode of around 1.1 (0.1 – 5.2)
746 Tg CH_4 yr^{-1} in the pan-Arctic budget- and would imply a mis-apportionment of CH_4 fluxes within
747 bottom-up budgeting efforts. It is likely that many bottom-up emission estimates do not accurately
748 account for the areal disproportionality of CH_4 hotspot fluxes within emitting surfaces and over-
749 allocate elevated flux rates during upscaling to areas that actually emit much less CH_4. This leads
750 to an overestimation of the contributing area to total study domain emissions, which is consistent
751 with the propensity of bottom-up emissions accounting to overshoot top-down constraints
752 (Thornton et al., 2016). For instance, regional lake CH_4 emissions, based on satellite remote
753 sensing analyses, were lower compared to previous estimates based on upscaling from individual
754 lakes (Engram et al., 2020). The high-spatial resolution CH_4 hotspot mapping ability of AVIRIS-
755 NG has the potential to improve CH_4 upscaling efforts by explicitly defining the areal extent of
756 high emission sites.

757 To be clear, although the hotspots described in this work may be a newly known CH_4
758 source to the atmosphere, at the current state of our collective understanding, it appears impossible
759 to determine whether this source is truly new with respect to the Arctic's response to recent
760 warming. Despite this incomplete understanding, our estimate serves as an important starting point
761 to motivate further investigation into thermokarst CH_4 emissions across the warming pan-Arctic
762 region.

763 If thermokarst CH_4 hotspot emissions are sourced primarily from ancient permafrost C
764 reservoirs, they likely also represent a new source to actively cycling C at the surface and an
765 enhancement to the positive C-climate feedback to further atmospheric warming. While this effect
766 remains difficult to quantify, recent model estimates suggest that thousands of Tg of CH_4 could be
767 released from abruptly thawing permafrost under RCP 8.5 warming scenarios by the end of the

768 century (Turetsky et al., 2020). The resulting increase in net radiative forcing by year 2300 (0.15
769 W m^{-2}) would represent roughly 1/3 of all CH_4-driven radiative forcing since 1750 (0.48 ± 0.05 W
770 m^{-2}) (Myhre et al., 2013). This emphasizes the importance of improving monitoring capabilities
771 for detecting and attributing permafrost C losses, especially as CH_4.
772

773 ## 5. Conclusions

774 We combined airborne and ground-based observations to quantify thermokarst CH_4
775 emissions on scales bridging chamber flux observations (< 1 m^2), plot-level monitoring (10 - 1000
776 of m^2), and thermokarst lake ecosystem flux budgeting (1-5 ha). Leveraging regional CH_4 hotpot
777 statistics from our 70,000 km^2 (7 Mha) AVIRIS-NG survey across Alaska and northwestern
778 Canada, we extrapolated our results to the pan-Arctic (18 Mkm^2).

779 Repeat AVIRIS-NG airborne measurements were used to detect a persistent, previously
780 undiscovered CH_4 hotspot along the shore of the Eastside Pond, an arm of Big Trail Lake, an
781 intensively thermokarst lake in Interior Alaska (Figure 1). Flux chamber measurements validated
782 the remote hotspot detection, yielding a mean daily flux of 1,170 mg CH_4 m^{-2} d^{-1}, with daily
783 maxima extending up to an extreme value of 24,200 mg CH_4 m^{-2} d^{-1} (Figures 2 & 3, Table 1).
784 Ground-based geophysical surveys of the BTL and Eastside Pond environment confirmed the
785 presence of actively thawing permafrost collocated at the CH_4 hotspot (Figure 4). We performed
786 an image classification of the BTL study area using AVIRIS-NG imagery, and used the resulting
787 map to apportion multiyear chamber-based CH_4 fluxes to the nine unique surface types observed
788 in the lake and nearshore environment (Figure 5). This contextualized the hotspot fluxes within
789 the broader lake environment, where we found that they comprised 40% of the study area diffusive
790 CH_4 emissions despite arising from less than 1% of the total study area.

An analysis of 65 AVIRIS-NG flight lines acquired during the ABoVE airborne campaigns in 2017, 2018, and 2019 (Elder, Thompson et al., 2020; C. E. Miller et al., 2019) revealed greater hotspot occurrence in regions exhibiting very high wetland and/or lake thermokarst occurrence (Figure 6). These hotspots all corresponded to CH_4 signals as large or larger than those observed from the Big Trail Lake hotspot. The relative fractions of CH_4 hotspot area in the lower panel of Figure 6 support our hypothesis that thermokarst processes promote extreme CH_4 emissions from disproportionately small areas in the Arctic permafrost landscape. To estimate CH_4 hotspot emissions from thermokarst regions across the pan-Arctic, we combined the mean of daily maximum fluxes from the Eastside Pond thermokarst hotspot with domain-wide hotspot occurrence statistics derived from the 70,000 km^2 AVIRIS-NG survey. We conservatively estimate that thermokarst hotspots emit roughly 1.1 Tg CH_4 yr^{-1} or roughly 4% of the current pan-Arctic wetland budget based on two independent estimation approaches.

This investigation highlights the unique insights made possible from the nine orders of magnitude in spatial scales sampled by the AVIRIS-NG airborne CH_4 hotspot imagery. Individual pixels (typically 25 m^2 or $2.5x10^{-5}$ km^2) resolve fine-scale geomorphological drivers while composite maps (1,000 – 10,000 km^2) enable the evaluation of climatic-scale influence on CH_4 emissions. The opportunity to simultaneously analyze hotspot patterns and statistics across site, landscape, and regional spatial scales enables us to characterize emergent properties and verify upscaling assumptions directly with observational data. One can also derive land surface classifications as well as vegetation traits and taxonomy from the same AVIRIS-NG pixels used to retrieve the CH_4 hot spots, resulting in exact collocation of these properties for correlation studies of unprecedented detail. Our initial analyses give us confidence that these types of multi-scale studies will help us overcome the scaling challenges that have long hindered accurate

estimates of the Arctic CH_4 budget (McGuire et al., 2012, 2018) and the Arctic System more generally (Vörösmarty et al., 2010). We continue to explore all dimensions of the AVIRIS-NG CH_4 hotspot dataset and anticipate more discoveries as we investigate biotic (i.e., vegetation, microbial, beaver activity, etc.) and abiotic (i.e., fire, hydrology, surficial geology, geomorphology, etc.) responses to thawing permafrost in a warming world.

Data Availability

AVIRIS-NG level 1 and level 2 radiance data are available via the Oak Ridge National Laboratory Distributed Active Archive Center (ORNL DAAC) at: https://daac.ornl.gov/ABOVE/guides/ABoVE_Airborne_AVIRIS_NG.html. In situ 2019 CH_4 flux data will also be published at ORNL DAAC before time of publication (DOI pending).

Conflict of Interest Statement

The authors declare no conflicts of interest pertaining to this work.

Acknowledgements

We would like to thank Michael Eastwood (JPL), John Chapman (JPL), Mark Helmlinger (JPL), and the rest of the AVIRIS-NG technical support and flight crew for spectroscopic data acquisition from the air and the ground. We thank the Alaska Satellite Facility (Univ. Alaska Fairbanks) for expedient AVIRIS-NG data transfer to servers at JPL, which enabled overnight detection of CH_4 hotspots at BTL. We acknowledge our ABoVE collaborators, David Butman (Univ. Washington), Mark Dornblaser (USGS), Kim Wikland (USGS), Rob Striegl (USGS), Catherine Kuhn (Univ. Washington), and Merritt Turetsky (Univ. Colorado) for their valuable feedback regarding several aspects of this work. We also thank Sarah Sackett and Dan Hodgkinson for logistical assistance through the ABoVE Fairbanks office. NASA funding was provided to PI C.E. Miller from the Terrestrial Ecology Program via ABoVE and C.D. Elder via USRA and the NASA Postdoctoral Program. USGS funding was provided by the USGS Land Change Science and Biological Sequestration Programs. The research was carried out at the Jet Propulsion Laboratory, California Institute of Technology, under a contract with the National Aeronautics and Space Administration.

References

Andresen, C. G., Lara, M. J., Tweedie, C. E., & Lougheed, V. L. (2017). Rising plant-mediated methane emissions from arctic wetlands. *Global Change Biology*, *23*(3), 1128–1139. https://doi.org/10.1111/gcb.13469

Bloom, A., Bowman, W. K., Lee, M., Turner, J. A., Schroeder, R., Worden, R. J., et al. (2017). A global wetland methane emissions and uncertainty dataset for atmospheric chemical transport models (WetCHARTs version 1.0). *Geoscientific Model Development*, *10*(6), 2141–2156. https://doi.org/10.5194/gmd-10-2141-2017

Briggs, M. A., Campbell, S., Nolan, J., Walvoord, M. A., Ntarlagiannis, D., Day-Lewis, F. D., & Lane, J. W. (2017). Surface Geophysical Methods for Characterising Frozen Ground in Transitional Permafrost Landscapes. *Permafrost and Periglacial Processes*, *28*(1), 52–65. https://doi.org/10.1002/ppp.1893

Cooper, M. D. A., Estop-Aragonés, C., Fisher, J. P., Thierry, A., Garnett, M. H., Charman, D. J., et al. (2017). Limited contribution of permafrost carbon to methane release from thawing peatlands. *Nature Climate Change*, *7*(7), 507–511. https://doi.org/10.1038/nclimate3328

Cusworth, D. H., Duren, R. M., Thorpe, A. K., Tseng, E., Thompson, D. R., Guha, A., et al. (2020). Using remote sensing to detect, validate, and quantify methane emissions from California solid waste operations. *Environmental Research Letters*, *15*(5). https://doi.org/10.1088/1748-9326/ab7b99

Dean, J. F., Meisel, O. H., Martyn Rosco, M., Marchesini, L. B., Garnett, M. H., Lenderink, H., et al. (2020). East Siberian Arctic inland waters emit mostly contemporary carbon. *Nature Communications*, *11*(1), 1–10. https://doi.org/10.1038/s41467-020-15511-6

Douglas, P. M. J., Gonzalez Moguel, R., Walter Anthony, K. M., Wik, M., Crill, P. M., Dawson,

K. S., et al. (2020). Clumped Isotopes Link Older Carbon Substrates With Slower Rates of Methanogenesis in Northern Lakes. *Geophysical Research Letters*, *47*(6), 1–10. https://doi.org/10.1029/2019GL086756

Duren, R. M., Thorpe, A. K., Foster, K. T., Rafiq, T., Hopkins, F. M., Yadav, V., et al. (2019). California's methane super-emitters. *Nature*, *575*(7781), 180–184. https://doi.org/10.1038/s41586-019-1720-3

Elder, C. D., Xu, X., Walker, J., Schnell, J. L., Hinkel, K. M., Townsend-Small, A., et al. (2018). Greenhouse gas emissions from diverse Arctic Alaskan lakes are dominated by young carbon. *Nature Climate Change*, *8*(2), 166–177. https://doi.org/10.1038/s41558-017-0066-9

Elder, C. D., Hanke, P. J., Walter Anthony, K. M., Thompson, D. R., Thorpe, A. K., & Miller, C. E. (2020). ABoVE: Methane Flux across Two Thermokarst Lake Ecosystems, Interior Alaska, 2018. ORNL DAAC, Oak Ridge, Tennessee, USA. https://doi.org/https://doi.org/10.3334/ORNLDAAC/1778

Elder, C. D., Thompson, D. R., Thorpe, A. K., Hanke, P., Walter Anthony, K. M., & Miller, C. E. (2020). Airborne Mapping Reveals Emergent Power Law of Arctic Methane Emissions. *Geophysical Research Letters*, *47*(3). https://doi.org/10.1029/2019GL085707

Engram, M., Anthony, K. M. W., Sachs, T., Kohnert, K., Serafimovich, A., Grosse, G., & Meyer, F. J. (2020). Remote sensing northern lake methane ebullition. *Nature Climate Change*. https://doi.org/10.1038/s41558-020-0762-8

Farquharson, L. M., Romanovsky, V. E., Cable, W. L., Walker, D. A., Kokelj, S. V., & Nicolsky, D. (2019). Climate Change Drives Widespread and Rapid Thermokarst Development in Very Cold Permafrost in the Canadian High Arctic. *Geophysical Research Letters*, *46*(12), 6681–6689. https://doi.org/10.1029/2019GL082187

892 Frankenberg, C., Thorpe, A. K., Thompson, D. R., Hulley, G., Kort, E. A., Vance, N., et al.
893 (2016). Airborne methane remote measurements reveal heavy-tail flux distribution in Four
894 Corners region. *Proceedings of the National Academy of Sciences*, *113*(35), 201605617.
895 https://doi.org/10.1073/pnas.1605617113
896 Hanna, S. R., Briggs, G. A., & Hosker, R. P. J. (1982). *Handbook on Atmospheric Diffusion*. (J.
897 S. Smith, Ed.) (Vol. TIC-11223). Technical Infromation Center, U.S. Department of
898 Energy.
899 James, S. R., Minsley, B. J., Pastick, N. J., & Sullivan, T. D. (2020). *Alaska permafrost*
900 *characterization: Geophysical and related field data collected from 2019-2020: U.S.*
901 *Geological Survey*. https://doi.org/https://doi.org/10.5066/P9I6VUQV
902 Jorgenson, M. T., Harden, J., Kanevskiy, M., O'Donnell, J., Wickland, K., Ewing, S., et al.
903 (2013). Reorganization of vegetation, hydrology and soil carbon after permafrost
904 degradation across heterogeneous boreal landscapes. *Environmental Research Letters*, *8*(3).
905 https://doi.org/10.1088/1748-9326/8/3/035017
906 Kass, M. A., Irons, T. P., Minsley, B. J., Pastick, N. J., Brown, D. R. N., & Wylie, B. K. (2017).
907 In situ nuclear magnetic resonance response of permafrost and active layer soil in boreal
908 and tundra ecosystems. *The Cryosphere Discussions*, *3*(January), 1–21.
909 https://doi.org/10.5194/tc-2016-256
910 Kleinberg, R. L., & Griffin, D. D. (2005). NMR measurements of permafrost: Unfrozen water
911 assay, pore-scale distribution of ice, and hydraulic permeability of sediments. *Cold Regions*
912 *Science and Technology*, *42*(1), 63–77. https://doi.org/10.1016/j.coldregions.2004.12.002
913 Kohnert, K., Juhls, B., Muster, S., Antonova, S., Serafimovich, A., Metzger, S., et al. (2018).
914 Toward understanding the contribution of waterbodies to the methane emissions of a

915 permafrost landscape on a regional scale- A case study from the Mackenzie Delta, Canada.
916 *Global Change Biology*, *00*(October 2017), 1–14. https://doi.org/10.1111/gcb.14289
917 Lewkowicz, A. G., & Way, R. G. (2019). Extremes of summer climate trigger thousands of
918 thermokarst landslides in a High Arctic environment. *Nature Communications*, *10*(1), 1–11.
919 https://doi.org/10.1038/s41467-019-09314-7
920 Lewkowicz, A. G., Etzelmüller, B., & Smith, S. L. (2016). Characteristics of Discontinuous
921 Permafrost based on Ground Temperature Measurements and Electrical Resistivity
922 Tomography, Southern Yukon, Canada. *Permafrost and Periglacial Processes*, *22*(4), 320–
923 342.
924 McGuire, A. D., Christensen, T. R., Hayes, D., Heroult, A., Euskirchen, E., Kimball, J. S., et al.
925 (2012). An assessment of the carbon balance of Arctic tundra: Comparisons among
926 observations, process models, and atmospheric inversions. *Biogeosciences*, *9*(8), 3185–
927 3204. https://doi.org/10.5194/bg-9-3185-2012
928 McGuire, A. D., Lawrence, D. M., Koven, C., Clein, J. S., Burke, E., Chen, G., et al. (2018).
929 Dependence of the evolution of carbon dynamics in the northern permafrost region on the
930 trajectory of climate change. *Proceedings of the National Academy of Sciences of the*
931 *United States of America*, *115*(15), 3882–3887. https://doi.org/10.1073/pnas.1719903115
932 Miller, C. E., Griffith, P. C., Goetz, S. J., Hoy, E. E., Pinto, N., McCubbin, I. B., et al. (2019).
933 An overview of ABoVE airborne campaign data acquisitions and science opportunities.
934 *Environmental Research Letters*, *14*, 080201.
935 Miller, S. M., Miller, C. E., Commane, R., Chang, R. Y. W., Dinardo, S. J., Henderson, J. M., et
936 al. (2016). A multiyear estimate of methane fluxes in Alaska from CARVE atmospheric
937 observations. *Global Biogeochemical Cycles*, *30*(10), 1441–1453.

https://doi.org/10.1002/2016GB005419

Minsley, B. J., Wellman, T. P., Walvoord, M. A., & Revil, A. (2015). Sensitivity of airborne geophysical data to sublacustrine and near-surface permafrost thaw. *Cryosphere*, *9*(2), 781–794. https://doi.org/10.5194/tc-9-781-2015

Minsley, B. J., Pastick, N. J., Wylie, B. K., Brown, D. R. N., & Kass, M. A. (2016). Journal of Geophysical Research : Earth Surface after fi re in boreal landscapes. *Journal of Geophysical Research: Earth Surface*, *121*, 320–335. https://doi.org/10.1002/2015JF003781.Received

Morel, X., Decharme, B., Delire, C., Krinner, G., Lund, M., Hansen, B. U., & Mastepanov, M. (2019). A New Process-Based Soil Methane Scheme: Evaluation Over Arctic Field Sites With the ISBA Land Surface Model. *Journal of Advances in Modeling Earth Systems*, *11*(1), 293–326. https://doi.org/10.1029/2018MS001329

Myhre, G., Shindell, D., Bréon, F.-M., Collins, W., Fuglestvedt, J., Huang, J., et al. (2013). Climate Change 2013: The Physical Science Basis. Contribution of Working Group I to the Fifth Assessment Report of the Intergovernmental Panel on Climate Change. In T. F. Stocker, D. Qin, G.-K. Plattner, M. Tignor, S. K. Allen, J. Boschung, et al. (Eds.), *Climate Change 2013: The Physical Science Basis. Contribution of Working Group I to the Fifth Assessment Report of the Intergovernmental Panel on Climate Change* (pp. 659–740). Cambridge: Cambridge University Press.

Olefeldt, D., Turetsky, M. R., Crill, P. M., & McGuire, A. D. (2013). Environmental and physical controls on northern terrestrial methane emissions across permafrost zones. *Global Change Biology*, *19*(2), 589–603. https://doi.org/10.1111/gcb.12071

Olefeldt, D., Goswami, S., Grosse, G., Hayes, D., Hugelius, G., Kuhry, P., et al. (2016).

961 Circumpolar distribution and carbon storage of thermokarst landscapes. *Nature*
962 *Communications*, *7*, 13043. https://doi.org/10.1038/ncomms13043
963 Peltola, O., Vesala, T., Gao, Y., Räty, O., Alekseychik, P., Aurela, M., et al. (2019). Monthly
964 Gridded Data Product of Northern Wetland Methane Emissions Based on Upscaling Eddy
965 Covariance Observations. *Earth System Science Data Discussions*, *11*, 1263–1289.
966 https://doi.org/10.5194/essd-2019-28
967 Roberts, D. A., Gardner, M., Church, R., Ustin, S., Scheer, G., & Green, R. O. (1998). Mapping
968 chaparral in the Santa Monica Mountains using multiple endmember spectral mixture
969 models. *Remote Sensing of Environment*, *65*(3), 267–279. https://doi.org/10.1016/S0034-
970 4257(98)00037-6
971 Schuur, E. A. G., McGuire, A. D., Schädel, C., Grosse, G., Harden, J. W., Hayes, D. J., et al.
972 (2015). Climate change and the permafrost carbon feedback. *Nature*, *520*(7546), 171–179.
973 https://doi.org/10.1038/nature14338
974 Sepulveda-Jauregui, A., Walter Anthony, K. M., Martinez-Cruz, K., Greene, S., & Thalasso, F.
975 (2015). Methane and carbon dioxide emissions from 40 lakes along a north–south
976 latitudinal transect in Alaska. *Biogeosciences*, *12*(11), 3197–3223.
977 https://doi.org/10.5194/bg-12-3197-2015
978 Serikova, S., Pokrovsky, O. S., Laudon, H., Krickov, I. V., Lim, A. G., Manasypov, R. M., &
979 Karlsson, J. (2019). High carbon emissions from thermokarst lakes of Western Siberia.
980 *Nature Communications*, *10*(1), 1–7. https://doi.org/10.1038/s41467-019-09592-1
981 Ström, L., Ekberg, A., Mastepanov, M., & Christensen, T. R. (2003). The effect of vascular
982 plants on carbon turnover and methane emissions from a tundra wetland. *Global Change*
983 *Biology*, *9*(8), 1185–1192. https://doi.org/10.1046/j.1365-2486.2003.00655.x

Sweeney, C., Dlugokencky, E., Miller, C. E., Wofsy, S., Karion, A., Dinardo, S., et al. (2016). No significant increase in long-term CH4 emissions on North Slope of Alaska despite significant increase in air temperature. *Geophysical Research Letters*, *43*, 1–8. https://doi.org/10.1002/2016GL069292

Sweeney, C., Chatterjee, A., Wolter, S., Mckain, K., Bogue, R., Newberger, T., et al. (2020). Atmospheric carbon cycle dynamics over the ABoVE domain: an integrated analysis using aircraft observations (Arctic-CAP) and model simulations (GEOS). *Atmospheric Chemistry and Physics Discussions*, (September), 1–30.

Theiler, J. (2012). The incredible shrinking covariance estimator. *Automatic Target Recognition XXII*, *8391*(May), 83910P-83910P–12. https://doi.org/10.1117/12.918718

Thompson, D. R., Gao, B. C., Green, R. O., Roberts, D. A., Dennison, P. E., & Lundeen, S. R. (2015). Atmospheric correction for global mapping spectroscopy: ATREM advances for the HyspIRI preparatory campaign. *Remote Sensing of Environment*, *167*, 64–77. https://doi.org/10.1016/j.rse.2015.02.010

Thompson, D. R., Leifer, I., Bovensmann, H., Eastwood, M., Fladeland, M., Frankenberg, C., et al. (2015). Real-time remote detection and measurement for airborne imaging spectroscopy: A case study with methane. *Atmospheric Measurement Techniques*, *8*(10), 4383–4397. https://doi.org/10.5194/amt-8-4383-2015

Thompson, D. R., Thorpe, A. K., Frankenberg, C., Green, R. O., Duren, R., Guanter, L., et al. (2016). Space-based remote imaging spectroscopy of the Aliso Canyon CH4 superemitter. *Geophysical Research Letters*, *43*(12), 6571–6578. https://doi.org/10.1002/2016GL069079

Thornton, B. F., Wik, M., & Crill, P. M. (2016). Double-counting challenges the accuracy of high-latitude methane inventories. *Geophysical Research Letters*, *43*(24), 12,569-12,577.

https://doi.org/10.1002/2016GL071772

Thornton, B. F., Prytherch, J., Andersson, K., Brooks, I. M., Salisbury, D., Tjernström, M., & Crill, P. M. (2020). Shipborne eddy covariance observations of methane fluxes constrain Arctic sea emissions. *Science Advances*, *6*(5), 1–11. https://doi.org/10.1126/sciadv.aay7934

Thorpe, A. K., Roberts, D. A., Bradley, E. S., Funk, C. C., Dennison, P. E., & Leifer, I. (2013). High resolution mapping of methane emissions from marine and terrestrial sources using a Cluster-Tuned Matched Filter technique and imaging spectrometry. *Remote Sensing of Environment*, *134*, 305–318. https://doi.org/10.1016/j.rse.2013.03.018

Thorpe, A. K., Frankenberg, C., & Roberts, D. A. (2014). Retrieval techniques for airborne imaging of methane concentrations using high spatial and moderate spectral resolution: Application to AVIRIS. *Atmospheric Measurement Techniques*, *7*(2), 491–506. https://doi.org/10.5194/amt-7-491-2014

Thorpe, A. K., Frankenberg, C., Aubrey, A. D., Roberts, D. A., Nottrott, A. A., Rahn, T. A., et al. (2016). Mapping methane concentrations from a controlled release experiment using the next generation airborne visible/infrared imaging spectrometer (AVIRIS-NG). *Remote Sensing of Environment*, *179*(June), 104–115. https://doi.org/10.1016/j.rse.2016.03.032

Thorpe, A. K., Duren, R. M., Conley, S., Prasad, K. R., Bue, B. D., Yadav, V., et al. (2020). Methane emissions from underground gas storage in California. *Environmental Research Letters*, *15*(4), 045005. https://doi.org/10.1088/1748-9326/ab751d

Turetsky, M., Abbott, B., Jones, M., Walter Anthony, K. M., Olefeldt, D., Schuur, E. A. G., et al. (2020). Carbon release through abrupt permafrost thaw. *Nature Geoscience*, *13*(2), 138–143. https://doi.org/10.1038/s41561-019-0526-0

Vörösmarty, C. J., McGuire, A. D., & Hobbie, J. E. (2010). *Scaling Studies in Arctic System*

Science and Policy Support. *U.S. Arctic Research Commission*.

Walsh, D., Turner, P., Grunewald, E., Zhang, H., Butler, J. J., Reboulet, E., et al. (2013). A small-diameter nmr logging tool for groundwater investigations. *Groundwater*, *51*(6), 914–926. https://doi.org/10.1111/gwat.12024

Walter Anthony, K. M., & Anthony, P. (2013). Constraining spatial variability of methane ebullition seeps in thermokarst lakes using point process models. *Journal of Geophysical Research: Biogeosciences*, *118*, 1015–1034. https://doi.org/10.1002/jgrg.20087

Walter Anthony, K. M., Vas, D. A., Brosius, L., Chapin III, F., Zimov, S., & Zhuang, Q. (2010). Estimating methane emissions from northern lakes using ice-bubble surveys. *Limnology and Oceanography: Methods*, *8*, 592–609. Retrieved from http://www.wap.aslo.orgwww.wap.aslo.org/lomethods/free/2010/0592.pdf

Walter Anthony, K. M., Anthony, P., Grosse, G., & Chanton, J. (2012). Geologic methane seeps along boundaries of Arctic permafrost thaw and melting glaciers. *Nature Geoscience*, *5*(6), 419–426. https://doi.org/10.1038/ngeo1480

Walter Anthony, K. M., Daanen, R., Anthony, P., Schneider Von Deimling, T., Ping, C. L., Chanton, J. P., & Grosse, G. (2016). Methane emissions proportional to permafrost carbon thawed in Arctic lakes since the 1950s. *Nature Geoscience*, *9*(9), 679–682. https://doi.org/10.1038/ngeo2795

Walter Anthony, K. M., Schneider von Deimling, T., Nitze, I., Frolking, S., Emond, A., Daanen, R., et al. (2018). 21St-Century Modeled Permafrost Carbon Emissions Accelerated By Abrupt Thaw Beneath Lakes. *Nature Communications*, *9*(1), 3262. https://doi.org/10.1038/s41467-018-05738-9

Walter, K. M., Chanton, J. P., Chapin, F. S., Schuur, E. a. G., & Zimov, S. a. (2008). Methane

production and bubble emissions from arctic lakes: Isotopic implications for source pathways and ages. *Journal of Geophysical Research*, *113*, G00A08. https://doi.org/10.1029/2007JG000569

Windsor, J., Moore, T. R., & Roulet, N. T. (1992). Episodic fluxes of methane from subarctic fens. *Canadian Journal of Soil Science*, *72*(4), 441–452. https://doi.org/10.4141/cjss92-037

Zona, D., Gioli, B., Commane, R., Lindaas, J., Wofsy, S. C., Miller, C. E., et al. (2015). Cold season emissions dominate the Arctic tundra methane budget. *Proceedings of the National Academy of Sciences of the United States of America*, *113*(1), 40–45. https://doi.org/10.1073/pnas.1516017113